Hydrodynamic performance of a Comb-Type Breakwater-WEC system: an analytical study

Abstract: A breakwater-WEC system combining heaving body Wave Energy Converters (WEC) and Comb-Type Breakwater (CTB) was investigated. The traditional CTB consists of a distributed array of separated bottom-mounted caissons and wave chambers are located between two caissons. Heaving bodies provide the power take off (PTO) principles that are located at the wave chamber of the CTB. The interaction of the CTB and WEC was investigated based on the linear potential flow theory. An analytical model has been developed to examine the hydrodynamic performance of CTB-WEC system. The analytical model is validated with results from an experimental study. Results show that an increase in conversion efficiency is observed when the device is located in the aft end of the wave chamber. A high efficiency (i.e., 77.4%) and qualified wave attenuation performance of the integrated system are achieved for the proposed CTB-WEC system. The wave resonance along the incident wave direction in the wave chamber is beneficial for wave energy capturing. Furthermore, it was found that the critical value k_c corresponds to the wave resonance, perpendicular to the incident wave direction, out of the wave chamber. The property of efficiency mitigation at regions of $k>k_c$ should be avoided while designing such a system.

Keywords: Comb-Type Breakwater; Wave Energy Converter, energy conversion efficiency, transmission coefficient; wave resonance; analytical investigation.

1 Introduction

The need for energy is growing rapidly. Many researchers and engineers pay attention to renewable energy resources. Wave power is a promising alternative to generate electricity with a low carbon impact. According to the energy conversion principles, categories of wave energy conversion system consist of attenuator, oscillating water column (OWC), overtopping system and point absorber (Wilberforce et al., 2019). Most of the devices are in the stage of laboratory tests and pre-commercial demonstration trails (Zhao and Ning, 2018; Brito-Melo et al., 2007). Barriers that affect commercialization of wave energy converters (WECs) include technological

challenges, economic, social and environmental concerns (Mustapa et al., 2017; Melikoglu, 2018; Cascajo et al., 2019).

Integrating WECs with marine structures potentially enhances economic viability through dual-functionality (Ji and Yuan, 2015; Zhao et al., 2019; Reabroy et al., 2019), including breakwater-WEC integrations (He et al., 2019; Zheng et al., 2019; Zhao et al., 2019), floating wind turbine-WEC integration (Pérez-Collazo et al., 2015), Eco Wave System (Tul Huda Ahmad et al., 2019), et al. The approach of combing WECs and breakwater provides a method to tackle the economic issues of WECs (Mustapa et al., 2017). The breakwater is frequently exposed to ocean waves, which provides a natural opportunity for wave energy utilization (Liu et al., 2012; Liu and Lin, 2013; Liu and Faraci, 2014). The integration systems composed of breakwater and WECs had been widely investigated (Ning et al., 2016; Kuo et al., 2017; Moretti et al., 2020; Chen et al., 2020; Zhang et al., 2020a and 2020b). Some concepts had been put into engineering, including sea-wave slot-cone generator (Margheritini et al., 2009), overtopping breakwater for wave energy conversion (Vicinanza et al., 2014) and breakwater-OWC in Mutriku (Henriques et al., 2017). Some novel concepts were also investigated numerically and experimentally, such as the pile-restrained floating breakwaters (Zhao and Ning, 2018), the Berkeley Wedge (Madhi and Yeung, 2018) and the ShoWED (Martinelli et al., 2016). Functions of the wave attenuation and energy utilization can be realized simultaneously for a hybrid breakwater-WEC system.

The Comb-Type Breakwater (CTB) is a new concept of the vertical breakwater, consisting of rectangular caissons and vertical side plates. The CTB dissipates the incident wave energy and reduces the total wave force compared with the conventional caisson breakwaters, which enhances the economic viability (Niu et al., 2003; Zhang et al., 2005). Fernyhough and Evans (1995) carried out multi-modal scattering properties of a periodic array of identical rectangular barriers separated by gaps, which is like the CTB. Hydrodynamic characteristics of the CTB was investigated experimentally (Li et al., 2002; Dong et al., 2003; Niu et al., 2018; Chen et al., 2019), numerically (Fang et al., 2010 and 2012; Zang et al., 2018) and analytically (Wang et al., 2018 and 2019). The relative wave amplitude in the wave chamber of the CTB increases to

some extent. The wave chamber could be considered as the wave energy gathering chamber, which enhances wave energy density.

Approaches that achieving wave amplification in the field of wave energy utilization include i) wave reflection wall (Sarkar et al., 2015; Michele et al., 2016; Howe and Nader, 2017), ii) wave contraction wall (Miao et al., 2005; Lovas et al., 2010; Parmeggiani et al., 2013; Saadat et al., 2013 and 2016; Deng et al., 2014; Ram et al., 2016; Zhang and Ning, 2019), iii) projecting wall with wave resonance (Count, 1984; Ikoma et al., 2016; Daniel Raj et al., 2019) and iv) wave amplification bottom topography (Rezanejad et al., 2013; Rezanejad et al., 2019). Saadat et al. (2016) proposed a novel Helmholtz Wave Energy Converter (HWEC), which amplifies the wave amplitude of a basin. The HWEC is designed to capture an augmented quantity of the wave power by using WECs. In summary, the integration of the CTB and WECs similar to HWEC may utilize the wave power in the wave chamber, which could improve the energy conversion efficiency of the WEC.

In this study, we proposed a novel integrated system consisting of an oscillating heaving WEC and a CTB, where the CTB is the base structure. An oscillating heaving PTO system is integrated between the adjacent caissons without modifying the geometry of the CTB base structure. The heaving PTO system is connected to a mechanical transmission system, which is similar to that described in Ning et al. (2016). The PTO system allows to capture the kinetic energy from the incident wave applying a heaving buoy. Due to the dual effect of wave energy absorbing of the WEC and the wave reflection of the CTB, the integrated system is anticipated to work effectively as a breakwater. Therefore, the wave energy gathering performance of the CTB and the magnitude of the PTO damping will be the key factors that affect the motion of WEC and transmission coefficient of the integrated system.

The paper aims to investigate numerically the hydrodynamic performance of a hybrid CTB, integrating a heaving WEC. The matching eigenfunction expansion method is used to solve the diffraction and radiation problems. The analytical model is validated for the energy conversion principle and with an experimental study.

This paper is organized as follows: Section 2 describes the mathematical model. Section 3

presents the validations of the analytical model. Section 4 presents the results and discussions. Lastly, the conclusions are given in Section 5.

2 Mathematical model

2.1 Problem description

The geometry of heaving bodies integrated into the CTB, as well as the arrangement of the cartesian coordinate system, are shown in Fig. 1. Noticeably, the flange of the CTB is not considered in the present study. Heaving bodies are arranged in wave chambers composed of adjacent caissons. Due to the periodicity of the integrated system, the problem can be reduced to an analogous channel problem with impermeable sidewalls. An array of the caisson-type breakwater with oscillating bodies is simplified as an integrated system unit, consisting of two caissons and a heaving body. All dimensions are presented as dimensionless units without loss of generality. A 3D cartesian coordinate system (o-xyz) is employed. The center of the origin is located at the cross-point of the still water surface and the medial axis of the breakwater and a heaving body. The z-axis is positive in the vertically upward direction. In order to capture wave power energy efficiently, it is assumed that a heaving body of width $2w_2$ is identical to the breadth of the wave chamber. A heaving body of length $2b_2$ is placed at a distance $2b_1$ and $2b_3$ from the back and the front wall of the caisson, respectively. A draft d_1 is assumed at the finite depth h. The caisson length along and perpendicular to the incident wave direction are $2B$ and $2w_1$. In the following text, symbols are expressed as $l=w_1+w_2$, $r_1=b_1+b_2$, $r_2=2b_1+b_2$, $r_3=b_2+b_3$ and $r_4=b_2+2b_3$. The mass M and stiffness K term are expressed as

$$M=4w_2b_2\rho d_1, \tag{1}$$

$$K=4w_2b_2\rho g, \tag{2}$$

where ρ and g represent the density of water and the acceleration due to gravity. The incident wave amplitude, height, wavelength and period are A, H_0, L and T.

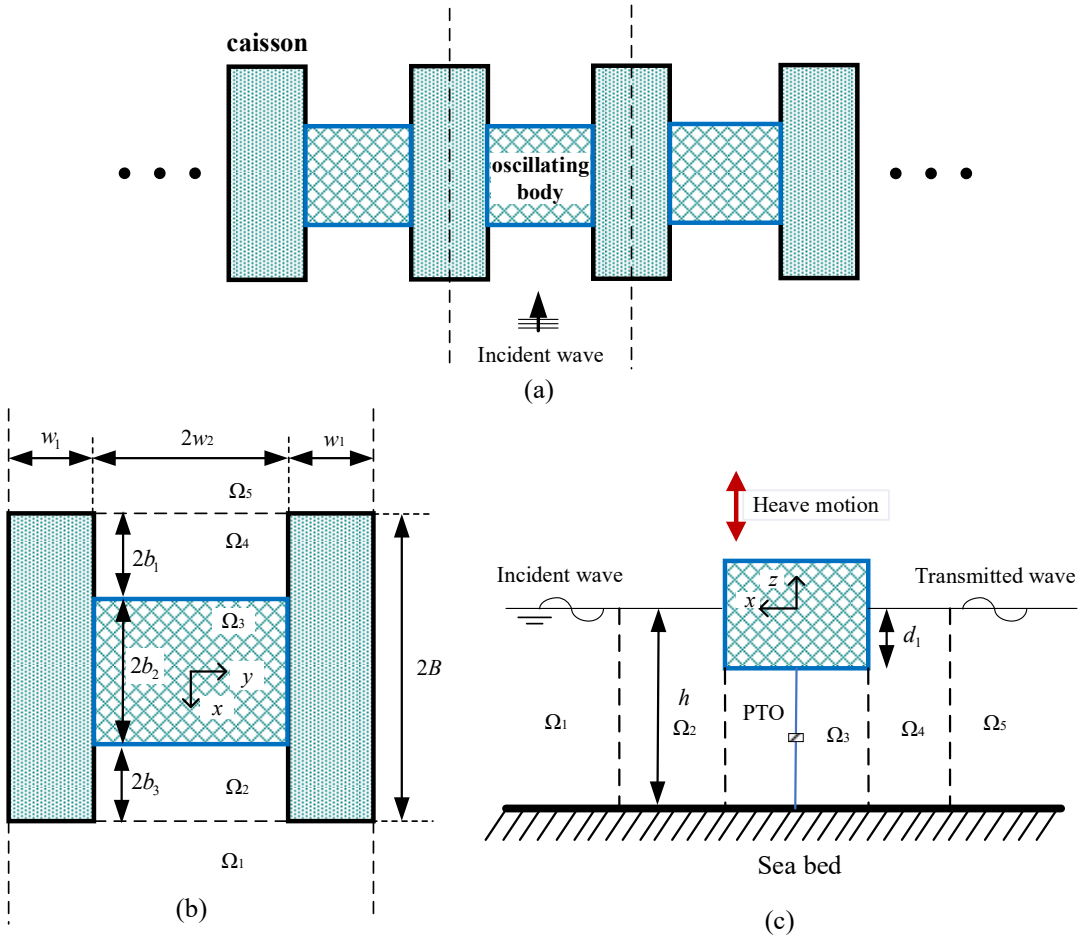

Fig. 1. (a) the layout of integrated system array, (b) the top view of the integrated system unit and (c) the vertical section of a heaving body-WEC.

2.2 Governing equation and boundary conditions

The fluid domain is divided into five subdomains (Fig. 1(b) and (c)), which are defined by Ω_i (i=1, 2, 3, 4 and 5) and given by Ω_1: $-l\le y\le l$, $r_4\le x\le+\infty$ and $-h\le z\le 0$; Ω_2: $-w_2\le y\le w_2$, $b_2\le x\le r_4$ and $-h\le z\le 0$; Ω_3: $-w_2\le y\le w_2$, $-b_2\le x\le b_2$ and $-h\le z\le -d_1$; Ω_4: $-w_2\le y\le w_2$, $-r_2\le x\le -b_2$ and $-h\le z\le 0$; Ω_5: $-l\le y\le l$, $-\infty\le x\le -r_2$ and $-h\le z\le 0$. The fluid is assumed as inviscid and incompressible. The motion is irrotational and simple harmonic in time angular frequency ω. The fluid motion in the whole domain is depicted by the spatial velocity potential:

$$\Phi(x,y,z,t)=\mathrm{Re}[\phi(x,y,z)\exp(-\mathrm{i}\omega t)], \tag{3}$$

where the spatial velocity potential $\phi(x, y, z)$ satisfies the three-dimensional Laplace equation

$$\frac{\partial^2\phi}{\partial x^2}+\frac{\partial^2\phi}{\partial y^2}+\frac{\partial^2\phi}{\partial z^2}=0. \tag{4}$$

Based on the consideration of the heave motion, ϕ_i is decomposed as

$$\phi_i = \phi_I + \phi_D^i + \phi_R^i, \tag{5}$$

where ϕ_D^i and ϕ_R^i are the diffraction and radiation potential of fluid domain Ω_i. ϕ_I, the incident potential, is defined as

$$\phi_I = -\frac{igA}{\omega}\frac{\cosh[\kappa_1(z+h_1)]}{\cosh(\kappa_1 h_1)}\exp^{-i\kappa_1(x-r_4)}, \tag{6}$$

where κ_1 is the wavenumber, determined by the dispersion relation $\omega^2=g\kappa_1\tanh(\kappa_1 h)$.

For the radiation problems, the radiation potential ϕ_R^i is expressed as

$$\phi_R^i = -i\omega\xi\varphi_R^i(x,y,z), \tag{7}$$

where ξ is the amplitude of heave motion and φ_R^i is the complex spatial velocity potential.

The governing equation and boundary conditions for the diffracted and radiated potentials can be written as

$$\frac{\partial\phi_D^i}{\partial z} - \frac{\omega^2}{g}\phi_D^i = 0 \text{ and } \frac{\partial\varphi_R^i}{\partial z} - \frac{\omega^2}{g}\varphi_R^i = 0 \quad (z=0, i=1,2,4,5), \tag{8}$$

$$\frac{\partial\phi_D^i}{\partial z} = 0 \text{ and } \frac{\partial\varphi_R^i}{\partial z} = 0 \quad (z=-h, i=1,2,3,4,5), \tag{9}$$

$$\frac{\partial\phi_D^i}{\partial z} = -\frac{\partial\phi_I}{\partial x} \text{ and } \frac{\partial\varphi_R^i}{\partial z} = 1 \quad (z=-d_1, i=3), \tag{10}$$

$$\frac{\partial\phi_D^i}{\partial y} = 0 \text{ and } \frac{\partial\varphi_R^i}{\partial y} = 0 \quad (y=\pm l, i=1,5), \tag{11}$$

$$\frac{\partial\phi_D^i}{\partial y} = 0 \text{ and } \frac{\partial\varphi_R^i}{\partial y} = 0 \quad (y=\pm w_2, i=2,3,4), \tag{12}$$

$$\lim_{r\to\pm\infty}\sqrt{r}\left(\frac{\partial}{\partial r} - i\kappa_1\right)\phi_D^i = 0 \text{ and } \lim_{r\to\pm\infty}\sqrt{r}\left(\frac{\partial}{\partial r} - i\kappa_1\right)\varphi_R^i = 0 \quad (i=1,5), \tag{13}$$

where $r=(x^2+y^2)^{1/2}$.

2.3 Solutions for wave diffraction and radiation problem

The velocity potentials for different regions can be derived based on the above-described boundary problems using the matching eigenfunction expansion method. Solving the governing equation along with boundary conditions described, spatial velocity potentials for each region can be written as

$$\phi_D^1 = -\frac{igA}{\omega}\left\{\sum_{m=1}^{\infty} C_m(y)\sum_{n=1}^{\infty} A_{mn} e^{p_{mn}(x-r_4)} Z_n(z)\right\}, \tag{14}$$

$$\phi_D^2 = -\frac{igA}{\omega}\left\{\sum_{m=1}^{\infty} \overline{C}_m(y)\sum_{n=1}^{\infty}\left(B_{mn}\frac{\cosh \overline{p}_{mn}(x-r_3)}{\cosh \overline{p}_{mn} b_3} + C_{mn}\frac{\sinh \overline{p}_{mn}(x-r_3)}{\sinh \overline{p}_{mn} b_3}\right) Z_n(z)\right\}, \tag{15}$$

$$\phi_D^3 = -\frac{igA}{\omega}\left\{\begin{array}{l}\left(D_{11} + E_{11}\frac{x}{b_2}\right) + \sum_{n=2}^{\infty}\left(D_{1n}\frac{\cosh q_{1n}x}{\cosh q_{1n}b_2} + E_{1n}\frac{\sinh q_{1n}x}{\sinh q_{1n}b_2}\right)\varphi_n(z) \\ + \sum_{m=2}^{\infty}\overline{C}_m(y)\sum_{n=1}^{\infty}\left(D_{mn}\frac{\cosh q_{mn}x}{\cosh q_{mn}b_2} + E_{mn}\frac{\sinh q_{mn}x}{\sinh q_{mn}b_2}\right)\varphi_n(z)\end{array}\right\} - \phi_1, \tag{16}$$

$$\phi_D^4 = -\frac{igA}{\omega}\left\{\sum_{m=1}^{\infty} \overline{C}_m(y)\sum_{n=1}^{\infty}\left(F_{mn}\frac{\cosh \overline{p}_{mn}(x+r_1)}{\cosh \overline{p}_{mn} b_1} + G_{mn}\frac{\sinh \overline{p}_{mn}(x+r_1)}{\sinh \overline{p}_{mn} b_1}\right) Z_n(z)\right\}, \tag{17}$$

$$\phi_D^5 = -\frac{igA}{\omega}\left\{\sum_{m=1}^{\infty} C_m(y)\sum_{n=1}^{\infty} H_{mn} e^{-p_{mn}(x+r_2)} Z_n(z)\right\}, \tag{18}$$

$$\varphi_R^1 = -\frac{igA}{\omega}\left\{\sum_{m=1}^{\infty} C_m(y)\sum_{n=1}^{\infty} A'_{mn} e^{p_{mn}(x-r_4)} Z_n(z)\right\}, \tag{19}$$

$$\varphi_R^2 = -\frac{igA}{\omega}\left\{\sum_{m=1}^{\infty} \overline{C}_m(y)\sum_{n=1}^{\infty}\left(B'_{mn}\frac{\cosh \overline{p}_{mn}(x-r_3)}{\cosh \overline{p}_{mn} b_3} + C'_{mn}\frac{\sinh \overline{p}_{mn}(x-r_3)}{\sinh \overline{p}_{mn} b_3}\right) Z_n(z)\right\}, \tag{20}$$

$$\varphi_R^3 = -\frac{igA}{\omega}\left\{\begin{array}{l}\left(D'_{11} + E'_{11}\frac{x}{b_2}\right) + \sum_{n=2}^{\infty}\left(D'_{1n}\frac{\cosh q_{1n}x}{\cosh q_{1n}b_2} + E'_{1n}\frac{\sinh q_{1n}x}{\sinh q_{1n}b_2}\right)\varphi_n(z) + \\ \sum_{m=2}^{\infty}\overline{C}_m(y)\sum_{n=1}^{\infty}\left(D'_{mn}\frac{\cosh q_{mn}x}{\cosh q_{mn}b_2} + E'_{mn}\frac{\sinh q_{mn}x}{\sinh q_{mn}b_2}\right)\varphi_n(z)\end{array}\right\} + \varphi_{R3P}^3, \tag{21}$$

$$\varphi_R^4 = -\frac{igA}{\omega}\left\{\sum_{m=1}^{\infty} \overline{C}_m(y)\sum_{n=1}^{\infty}\left(F'_{mn}\frac{\cosh \overline{p}_{mn}(x+r_1)}{\cosh \overline{p}_{mn} b_1} + G'_{mn}\frac{\sinh \overline{p}_{mn}(x+r_1)}{\sinh \overline{p}_{mn} b_1}\right) Z_n(z)\right\}, \tag{22}$$

$$\varphi_R^5 = -\frac{igA}{\omega}\left\{\sum_{m=1}^{\infty} C_m(y)\sum_{n=1}^{\infty} H'_{mn} e^{-p_{mn}(x+r_2)} Z_n(z)\right\}, \tag{23}$$

where $\varphi_{R3P}^3 = \dfrac{(z+h)^2 - x^2}{2(h-d_1)}$.

The unknown coefficients X_{mn} and X'_{mn}, for m and n=1, 2⋯, with $X \equiv \{A, B, \cdots, H\}$ and $X' \equiv \{A', B', \cdots, H'\}$. $Z_n(z)$ and $\varphi_n(z)$ are eigenfunctions in the z-direction and given by the following equation

$$Z_n(z)=\cos k_n(z+h)/\cos k_n h, \tag{24}$$

$$\varphi_n(z)=\cos \mu_n(z+h). \tag{25}$$

The k_n are the roots of dispersion relation in k as given by $\omega^2=-gk\tan(kh)$, where the dispersion relation has one imaginary root k_1 and the infinite number of positive real roots k_n, n=2, 3⋯, with $\mu_n=(n-1)\pi/(h-d_1)$, n=1, 2⋯. $C_m(y)$ and $\bar{C}_m(y)$ are eigenfunctions in the y-direction and given by the following equation

$$C_m(y)=\cos \gamma_m(l-y), \tag{26}$$

$$\bar{C}_m(y)=\cos \bar{\gamma}_m(w_2-y), \tag{27}$$

where $\gamma_m=(m-1)\pi/l$ and $\bar{\gamma}_m=(m-1)\pi/w_2$. The P_{mn}, $\bar{P}_{mn}$ and q_{mn} are defined as follows

$$p_{mn}=\begin{cases}-\sqrt{\lambda_{m1}}, \lambda_{m1}\geq 0, m=1,2,\cdots,\\ \mathrm{i}\sqrt{\lambda_{m1}}, \lambda_{m1}<0, m=1,2,\cdots,\\ -\sqrt{\lambda_{mn}}, m=1,2,\cdots, n=2,3,\cdots,\end{cases} \quad ,\lambda_{mn}=\left[(m-1)\pi/l\right]^2+k_n^2, \tag{28}$$

$$\bar{p}_{mn}=\begin{cases}\sqrt{\bar{\lambda}_{m1}}, \bar{\lambda}_{m1}\geq 0, m=1,2,\cdots,\\ \mathrm{i}\sqrt{\bar{\lambda}_{m1}}, \bar{\lambda}_{m1}<0, m=1,2,\cdots,\\ \sqrt{\bar{\lambda}_{mn}}, m=1,2,\cdots, n=2,3,\cdots,\end{cases} \quad ,\bar{\lambda}_{mn}=\left[(m-1)\pi/w_2\right]^2+k_n^2, \tag{29}$$

$$q_{mn}=\sqrt{\bar{\gamma}_m^2+\mu_n^2}. \tag{30}$$

Furthermore, the eigenfunctions $Z_n(z)$, $\varphi_n(z)$, $C_m(y)$ and $\bar{C}_m(y)$ satisfy the orthogonal relations.

$$\alpha_{nu}=\int_{-h}^{0} Z_n(z)Z_u(z)dz=\begin{cases}0, n\neq u,\\ \dfrac{1}{\cos^2 k_n h}\left(\dfrac{h}{2}+\dfrac{\sin 2k_n h}{4k_n}\right), n=u,\end{cases} \tag{31}$$

$$\bar{\sigma}_{mv}=\int_{-w_2}^{w_2}\bar{C}_m(y)\bar{C}_v(y)dy=\begin{cases}\delta_m w_2, m=v,\\ 0, m\neq v,\end{cases} \tag{32}$$

$$\sigma_{mv}=\int_{-l}^{l}C_m(y)C_v(y)dy=\begin{cases}\delta_m l, m=v,\\ 0, m\neq v,\end{cases} \tag{33}$$

where δ_1=2 and δ_m=1 for m=2, 3⋯,

$$U_{nu}=\int_{-h}^{-d_1}\varphi_n(z)\varphi_u(z)dz=\begin{cases}\tau_n(h-d_1), n=u,\\ 0, n\neq u,\end{cases} \tag{34}$$

where τ_1=1 and τ_n=1/2 for n=2, 3⋯.

The diffracted and radiated potentials satisfy the continuity conditions for both the normal velocity and pressure at the interfaces between adjacent subdomains:

A) On the interface between region Ω_1 and Ω_2 ($x=r_4$) through;

$$\phi_D^1 = \phi_D^2 \text{ and } \varphi_R^1 = \varphi_R^2, \text{ at } -w_2 < y < w_2, -h < z < 0 \tag{35}$$

$$\frac{\partial \phi_D^1}{\partial x} = \begin{cases} \dfrac{\partial \phi_D^2}{\partial x} \\ -\dfrac{\partial \phi_I}{\partial x} \end{cases} \text{ and } \frac{\partial \varphi_R^1}{\partial x} = \begin{cases} \dfrac{\partial \varphi_R^2}{\partial x}, \text{ at } -w_2 < y < w_2, -h < z < 0 \\ 0, \text{ at } (-l < y < -w_2) \cup (w_2 < y < l), -h < z < 0 \end{cases} \tag{36}$$

B) On the interface between region Ω_2 and Ω_3 ($x=b_2$) through;

$$\phi_D^2 = \phi_D^3 \text{ and } \varphi_R^2 = \varphi_R^3, -w_2 < y < w_2, -h < z < -d_1 \tag{37}$$

$$\frac{\partial \phi_D^2}{\partial x} = \begin{cases} \dfrac{\partial \phi_D^3}{\partial x} \\ -\dfrac{\partial \phi_I}{\partial x} \end{cases} \text{ and } \frac{\partial \varphi_R^2}{\partial x} = \begin{cases} \dfrac{\partial \varphi_R^3}{\partial x}, \text{ at } -w_2 < y < w_2, -h < z < -d_1 \\ 0, \text{ at } -w_2 < y < w_2, -d_1 < z < 0 \end{cases} \tag{38}$$

C) On the interface between region Ω_3 and Ω_4 ($x=-b_2$) through;

$$\phi_D^3 = \phi_D^4 \text{ and } \varphi_R^3 = \varphi_R^4, -w_2 < y < w_2, -h < z < -d_1 \tag{39}$$

$$\frac{\partial \phi_D^4}{\partial x} = \begin{cases} \dfrac{\partial \phi_D^3}{\partial x} \\ -\dfrac{\partial \phi_I}{\partial x} \end{cases} \text{ and } \frac{\partial \varphi_R^4}{\partial x} = \begin{cases} \dfrac{\partial \varphi_R^3}{\partial x}, \text{ at } -w_2 < y < w_2, -h < z < -d_1 \\ 0, \text{ at } -w_2 < y < w_2, -d_1 < z < 0 \end{cases} \tag{40}$$

D) On the interface between region Ω_4 and Ω_5 ($x=-r_2$) through.

$$\phi_D^4 = \phi_D^5 \text{ and } \varphi_R^4 = \varphi_R^5, \text{ at } -w_2 < y < w_2, -h < z < 0 \tag{41}$$

$$\frac{\partial \phi_D^5}{\partial x} = \begin{cases} -\dfrac{\partial \phi_I}{\partial x} \\ \dfrac{\partial \phi_D^4}{\partial x} \end{cases} \text{ and } \frac{\partial \varphi_R^5}{\partial x} = \begin{cases} 0, \text{ at } (-l < y < -w_2) \cup (w_2 < y < l), -h < z < 0 \\ \dfrac{\partial \varphi_R^4}{\partial x}, \text{ at } -w_2 < y < w_2, -h < z < 0 \end{cases} \tag{42}$$

Integrate velocity potentials in Eqs. (14~23) into both the velocity and pressure continuity conditions. We had multiplied both sides of Eqs. (35), (38), (40) and (41) by $\bar{C}_v(y)$ and $Z_u(z)$,

both sides of Eqs. (36) and (42) by $C_v(y)$ and $Z_u(z)$, and both sides of Eqs. (37) and (39) by $\bar{C}_v(y)$ and $\varphi_u(z)$. The matching eigenfunction expansion method and the orthogonal relations of the y-direction and z-direction eigenfunctions are applied to solve both i) the wave diffraction and ii) radiation problems. The Eqs. (35~42) represent a system of algebraic equations of unknowns X_{mn} and X'_{mn}. For the infinite series sums of m, v, n and u are truncated for the finite number m, $v=M_j$, and n, $u=N_j$, where j=1, 2⋯, 8. Thus, we have obtained $8M_jN_j$, where the algebraic equations are the same number of unknowns. The solution of the integrated system of equations determines the full solution of velocity potential, and all hydrodynamic quantities can be estimated.

2.4 Hydrodynamic quantities

The vertical exciting force F_z on a heaving body can be calculated by

$$F_z = \mathrm{i}\omega\rho\int_{S_b}(\phi_I+\phi_D)n_z\mathrm{d}s, \tag{43}$$

where S_b is the bottom surface of a heaving body and n_z is the unit normal vector in the positive z-direction. The added mass μ and radiation damping λ in the heave motion subjected to a unit forced motion of a heaving body can be written as

$$\mu = \rho\int_{S_b}\mathrm{Re}[\varphi_R]n_z\mathrm{d}s, \tag{44}$$

$$\lambda = \rho\omega\int_{S_b}\mathrm{Im}[\varphi_R]n_z\mathrm{d}s, \tag{45}$$

where Re[ ] and Im[ ] denote the real and imaginary part of a complex.

According to the motion equation in the frequency domain, the heave response amplitude ξ can be expressed as

$$\xi = \frac{F_z}{-\omega^2(M+\mu)-\mathrm{i}\omega(\lambda+\lambda_{PTO})+K}, \tag{46}$$

where λ_{PTO} is the Power Take-Off (PTO) damping. The heave RAO is defined as ξ/A. The optimal PTO damping of an isolated WEC can be expressed as

$$\lambda_{optimal} = \sqrt{(K/\omega-\omega(M+\mu))^2+\lambda^2}. \tag{47}$$

The Capture Width Ratio (CWR) η can be expressed as $\eta=P_{capture}/P_{incident}$, where $P_{capture}$ is the absorbed power of a WEC with the PTO damping λ_{PTO}, and $P_{incident}$ represents the incident

wave power with the incident wave width $2l$, corresponding to that of the integrated system.

$$P_{\text{capture}} = 0.5\lambda_{\text{PTO}}\omega^2\left|\xi\right|^2 \tag{48}$$

$$P_{\text{incident}} = \frac{1}{2}\frac{\rho g A^2 \omega l}{\kappa_1}\left(1+\frac{2\kappa_1 h}{\sinh 2\kappa_1 h}\right) \tag{49}$$

The hydrodynamic performance of an integrated system can be evaluated by reflection coefficient K_r and transmission coefficient K_t:

$$K_r = \begin{cases} \left|A_{11} - \mathrm{i}\omega\xi A'_{11}\right| & ,\kappa_1\pi < l \\ \sqrt{\left|A_{11} - \mathrm{i}\omega\xi A'_{11}\right|^2 + \sum_{m=2}^{p}\frac{\sqrt{\kappa_1^2 - \left[(m-1)\pi/l\right]^2}}{2\kappa_1}\left|A_{m1} - \mathrm{i}\omega\xi A'_{m1}\right|^2} & ,\kappa_1\pi \geq l \end{cases}, \tag{50}$$

$$K_t = \begin{cases} \left|1 + \left(H_{11} - \mathrm{i}\omega\xi H'_{11}\right)\right| & ,\kappa_1\pi < l \\ \sqrt{\left|1 + \left(H_{11} - \mathrm{i}\omega\xi H'_{11}\right)\right|^2 + \sum_{m=2}^{p}\frac{\sqrt{\kappa_1^2 - \left[(m-1)\pi/l\right]^2}}{2\kappa_1}\left|\left(H_{m1} - \mathrm{i}\omega\xi H'_{m1}\right)\right|^2} & ,\kappa_1\pi \geq l \end{cases}, \tag{51}$$

where p represents the orders of wavenumber which rounds down the $[\kappa_1 l/\pi + 1]$.

3 Validations

3.1 Validations using the law of energy conservation

Since the law of energy conservation is satisfied within the frame of the linear potential flow theory, the relation of $K_r^2+K_t^2+\eta=1$ is used to validate the present analytical model. Fig. 2 showed the variations of the K_r, K_t, η and $K_r^2+K_t^2+\eta$ with the dimensionless wavenumber for geometrical parameters of B/h=1/2, d_1/h=1/3, b_2/h=1/3, b_1/b_2=1/4, w_1/h=1/3 and l/h=2/3. The PTO damping is chosen as λ_{optimal}. Based on the numerical convergence analysis, the terms of the z- and y-direction eigenfunctions are truncated at N=5 and M=15, respectively. As indicated in Table 1 and Fig. 2, the relation of energy conservation is satisfied, which verifies the accuracy of the present analytical model.

Table 1. Results of the K_r, K_t, η and $K_r^2+K_t^2+\eta$.

kh	0.360	1.078	1.440	2.160	2.520	2.878	3.600
η	0.058326	0.206348	0.366226	0.243976	0.150712	0.104499	0.065484
K_r	0.467854	0.741117	0.635855	0.857654	0.917791	0.944509	0.965978
K_t	0.850168	0.494366	0.479022	0.143016	0.083354	0.058337	0.037451
$K_r^2+K_t^2+\eta$	1.000000	1.000000	1.000000	1.000000	1.000000	1.000000	1.000000

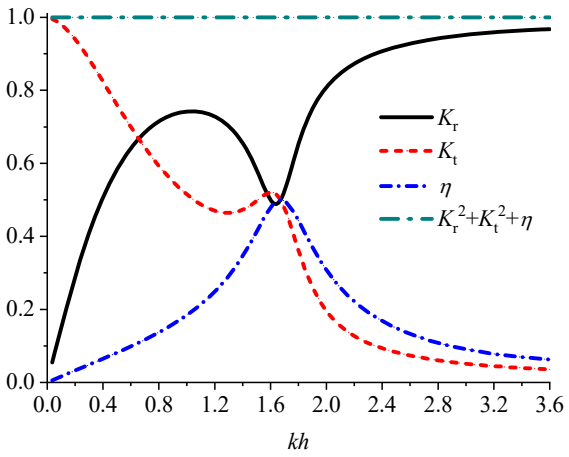

Fig. 2. Variations of reflection coefficient (K_r), transmission coefficient (K_t), capture width ratio (η) and $K_r^2+K_t^2+\eta$ versus dimensionless wavenumber.

3.2 Comparison between theoretical calculations and experimental data

In order to validate the analytical model, an experimental investigation was conducted in a wave flume at Harbin Engineering University. The experimental investigation focused on the heave response characteristics of the buoy and the transmission coefficient of the system. The dimensions of the flume were 33m in length, 0.8m in width and 1.0m in depth. Froude scaling a 1:20 model was applied for the experimental model. The length of a heaving body along and perpendicular to the incident wave was 0.39m and 0.36m (i.e., b_2=0.195m and w_2=0.18m), respectively. The height of the heaving buoy was 0.4m. The parameters of caissons were width B=0.3m, depth w_1=0.2m and height was 0.95m. The heaving body was arranged in the center of the wave chamber (i.e., b_1=b_3=0.0525m). In order to avoid unnecessary friction and possible collisions, a 1cm gap was set between each side of the caissons to the wave flume wall and a heaving body. The heaving body was constraint by two vertical guides (slide rails) located at the up- and down-wave side, restricting the oscillating body to move only in the heave direction by two pulleys. The dynamic signal test system with a draw-wire displacement sensor was used to monitor the heave motion. The friction coefficient between the pulley and slide rail is 0.078 (determined by a fiction coefficient measurement test). During the verification test, the still water depth h is fixed at 0.6m, the draft of the heaving body d_1=0.195m, the targeted incident wave height H_0=0.05m and the tested wave period vary from 1.1s to 1.6s (i.e., 1.1s, 1.2s, 1.3s, 1.4s and 1.6s). Fig. 3 shows the arrangement of the caissons and a heaving body.

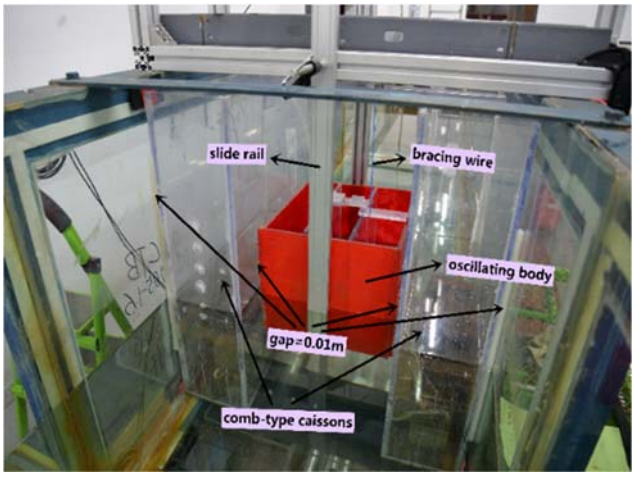

Fig.3. The arrangement of the caissons and a heaving body.

Considering the external damping b_{ext} (include the damping caused by fluid viscous effect and friction loss) obtained by free decay tests, the motion equation of a heaving body can be written as $(-\omega^2(M+\mu)-i\omega(\lambda+b_{ext})+K)\xi=F_z$. For the present investigation, the external damping is determined as 32.572kg/s. The hydrodynamic coefficients of the equation (μ, λ and F_z) can be derived from the present analytical model. Fig. 4 shows the comparison of the present analytical and experimental results. The RAO and transmission coefficient obtained by the analytical model agrees with the experimental data very well. The overall agreement verifies the present analytical model.

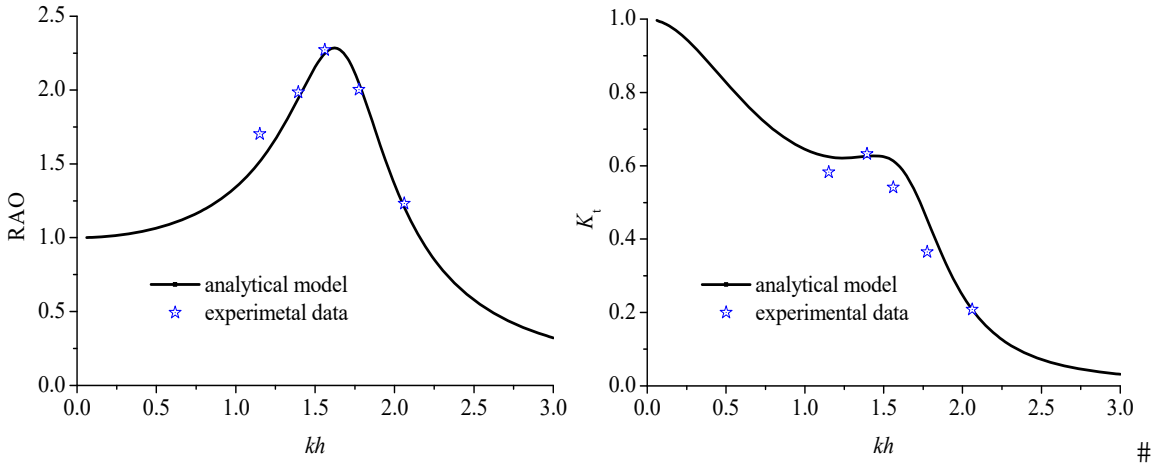

#

Fig. 4. The comparison of heave RAO and transmission coefficient K_t between the results of the analytical model and experimental data.

4 Results and discussions

The hydrodynamic performance of the system relies on several parameters including the

locations, size of a heaving body and the caisson.

4.1 Parametric study of the location and the size of a heaving body

4.1.1 Effect of the location of the device

As the wave absorption of a heaving body is affected by its locations in the wave chamber of a CTB, the power capture efficiency is affected, too. Fig. 5 shows the variations of the η, K_r and K_t against the dimensionless wavenumber (kh). Cases of $b_1/b_3=10^{-4}$, 1/5, 1/2, 1, 2 and 5 between the distance from a heaving body to the back and the front wall of the caisson are considered. The other parameters are kept constant as $b_2/h=1/3$, $w_1/h=1/4$, $l/h=1/2$, $d_1/h=1/3$ and $B/h=5/6$. The PTO damping of the device is selected as the optimal damping in Section 4. From Fig. 5(a), the CWR shows the parabola changes. Interestingly, as b_1/b_3 increases (i.e., the body is closer to the aft end of the wave chamber), the maximum of CWR decreases and frequencies corresponding to the peak of CWR shifts to the low-frequency region. The reflection coefficient experiences a dip at $1.5<kh<2.0$, accompanying the peak of the CWR. The opposite trend is found for that of the transmission coefficient. As is shown in Fig. 5(c), the location changes of a heaving body have little influence on the transmission coefficient. Comparatively, location changes of a heaving body obviously modify the reflection coefficient at $1.3<kh<2.8$, which reflects that the reflection coefficient increases with the increasing b_1/b_3.

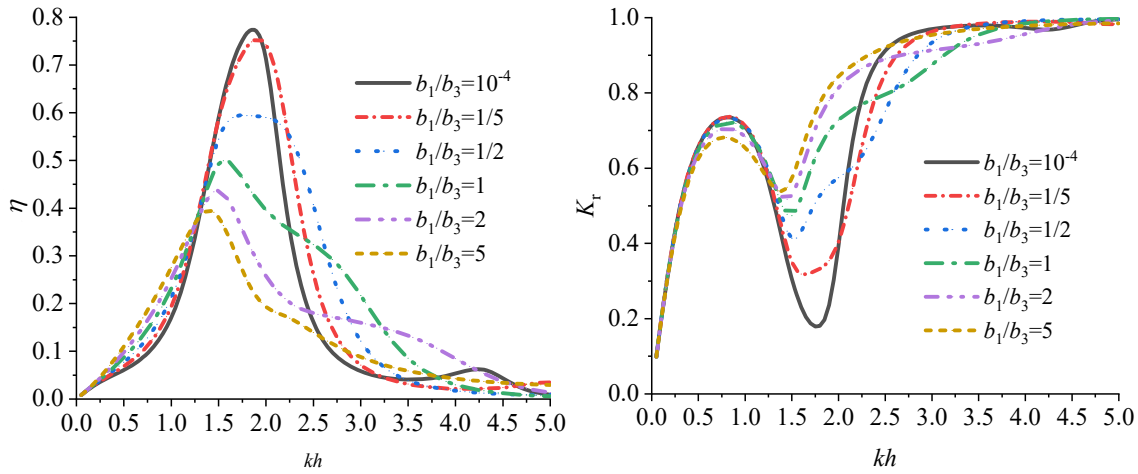

(a) (b)

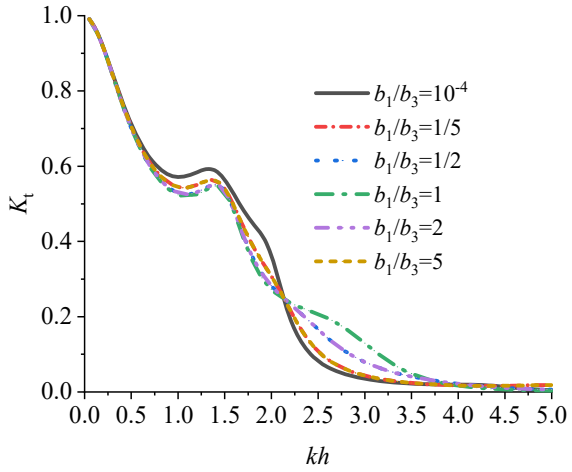

(c)

Fig. 5. Variations of (a) η, (b) K_r and (c) K_t versus kh for different cases ($b_1/b_3=10^{-4}$, 1/5, 1/2, 1, 2 and 5).

To further illustrate the effect of the locations of the device on the CWR of the system, the wave exciting force acting on the bottom of the device (F_z) and the relative wave amplitude in the wave chamber without a heaving body (ζ/A) are presented in Fig. 6. In the middle-frequency region ($1.2<kh<2.8$), the CWR approaches the peak value successively. The trend of the CWR vs kh is in accord with that of the F_z. Strong wave augmentation behavior in the wave chamber for different frequencies (kh=1.32, 1.45, 1.58, 1.76 and 1.90 which corresponds to the peak value of the CWR for the cases of b_1/b_3=5, 2, 1, 1/2 and 1/5, respectively) is found from Fig. 6(b). The cancellation of the device can be realized by setting the size of the device as a very small value (i.e., $d_1/h= b_2/h =10^{-5}$). The location of the relative wave amplitude peak in the wave chamber approaches to the aft end of the wave chamber as the dimensionless wavenumber increases. Note that the relative wave amplitude approaches maximum value at half breadth of wave chamber for only one case (as is shown in Fig. 10). Hence, the optimal location of the buoy (corresponding to the maximum efficiency) may be not the middle section. Besides, the changes of the location of the buoy also lead to the modification of the natural frequency of the buoy. Detailly, from Fig. 5(a) we can draw that the natural frequency generally decreases with the increasing of b_1/b_3. As is shown in Fig. 6(a), the smaller b_1/b_3, the greater the wave exciting force at natural frequency can be found. Wave exciting force plays an important role while estimating the efficiency of a heaving buoy. This may result in that the optimal location

corresponding to the maximal peak efficiency is the aft end.

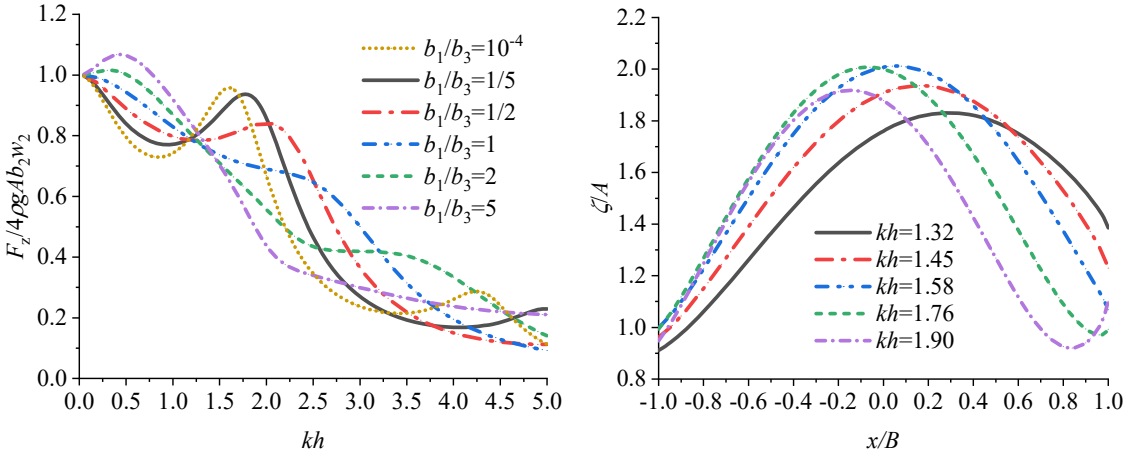

Fig. 6. Variations of (a) dimensionless wave exciting force ($F_z/4\rho gAb_2w_2$) versus kh for different locations of the device (b_1/b_3=10^{-4}, 1/5, 1/2, 1, 2 and 5) and (b) relative wave amplitude (ζ/A) in the wave chamber without a heaving body for different wavenumbers.

By comparing with the maximum efficiency η_{max} in cases of different b_1/b_3 (as shown in Fig. 5(a)), we found that η_{max} increases with the decreasing of the b_1/b_3. Specifically, compared with the cases at the bow end, the η_{max} becomes doubled approximately when the buoy is located at the aft end. A high efficiency of 77.4% can be achieved when the device is located at the aft end. This is obviously greater than that without the caissons, which corresponds to the 2D condition. The CWR maximum of a 2D symmetrical heaving device is 50% (Zhao et al., 2017). The advantages of the proposed system are that, compared with the original cases without caissons (i.e., the width of the device equals to CTB width perpendicular to the incident wave direction), the efficiency of the device is enhanced significantly even though the size of the device is narrow comparatively. The efficiency enhancement is due to the wave argumentation behavior of the CTB.

4.1.2 Effect of the size of the device

In this subsection, the effect of the draft and breadth (along the incident wave direction) of a heaving body is investigated. Fig. 7 and 8 present the results which may illustrate the effect of the draft and breadth of the heaving body, respectively. Overall, the modifications of the draft and breadth of the body slightly affect the trend of the CWR, K_r and K_t. Obviously, the draft

and the breadth of the heaving body affect the natural frequency of the heaving body and wave attenuation performance of the integrated system. The natural frequency shifts to the lower frequency region with the increasing draft and breadth. It was argued by Koutandos et al. (2005) that a better wave barrier performance can be realized for the system with a relatively large-size WEC device.

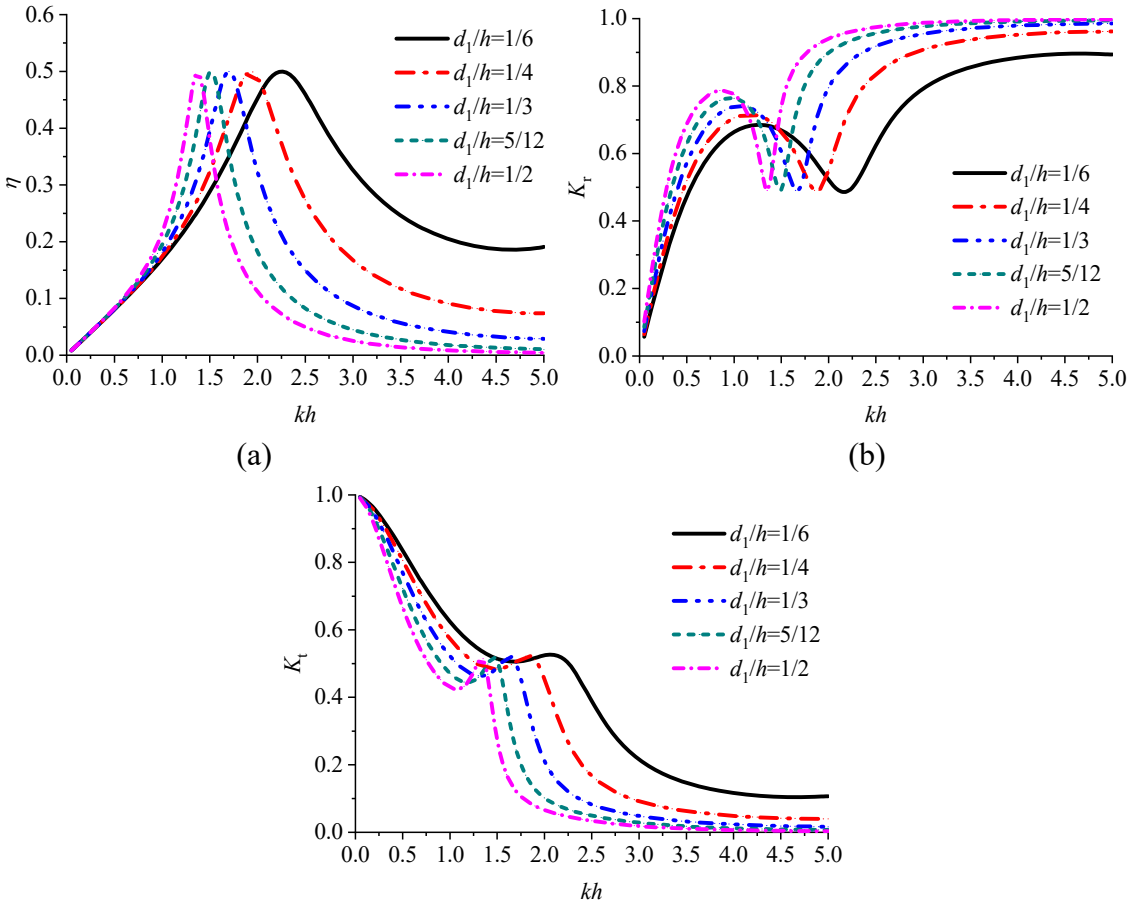

(a) (b)

(c)

Fig. 7. Variations of (a) η, (b) K_r and (c) K_t versus kh for different cases of drafts (B/h=1/2, b_2/h=1/3, b_1/b_3=1, w_1/h=1/4 and l/h=1/2, d_1/h is selected as 1/6, 1/4, 1/3, 5/12 and 1/2).

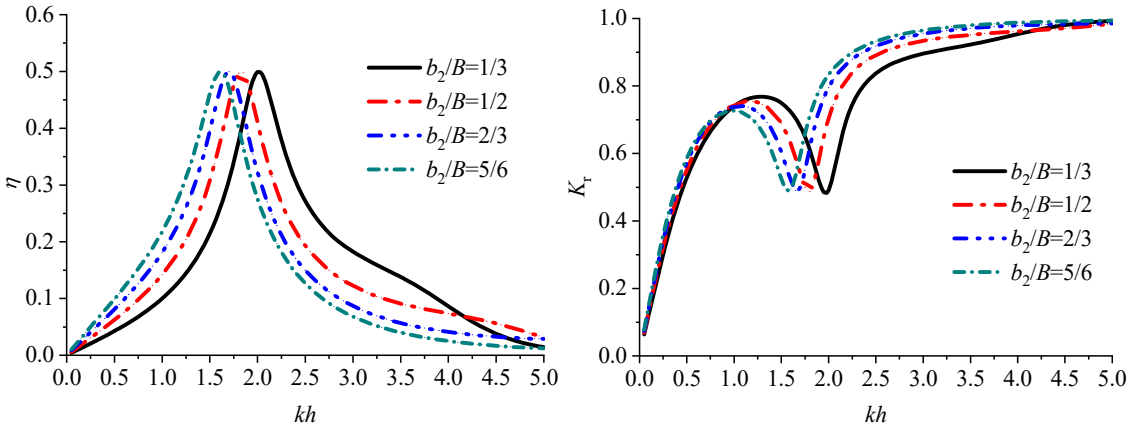

(a) (b)

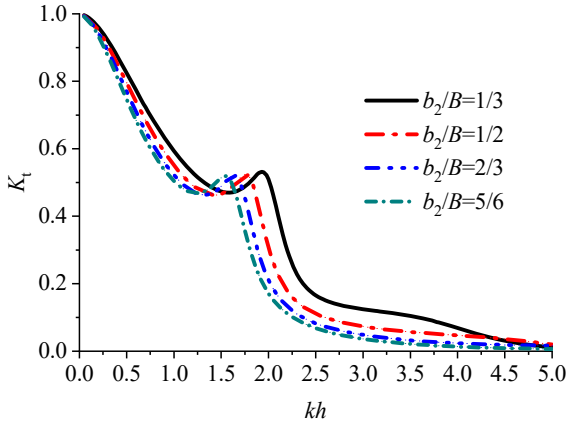

(c)

Fig. 8. Variations of (a) η, (b) K_r and (c) K_t versus kh for different cases of breadths (b_1/b_3=1, d_1/h=1/3, w_1/h=1/4, B/h=1/2, and l/h=1/2, b_2/B is selected as 1/3, 1/2, 2/3 and 5/6).

To illustrate the impact of WEC device on the hydrodynamic performance of the CTB, the results (K_r, K_t, CWR and wave amplification factor which is defined as $(\zeta\text{-}A)/A$) corresponding to the cases with and without the WEC device are analyzed and results are shown in Fig. 8. From Fig. 9, it can be found that the existence of the WEC device significantly mitigates the transmission coefficient and reflection coefficient over the whole frequency region. Specifically, considering the conditions K_t<0.5 and η>20%, the available frequency region is 2.25<kh<4.00 for the draft of d_1/h=1/6.

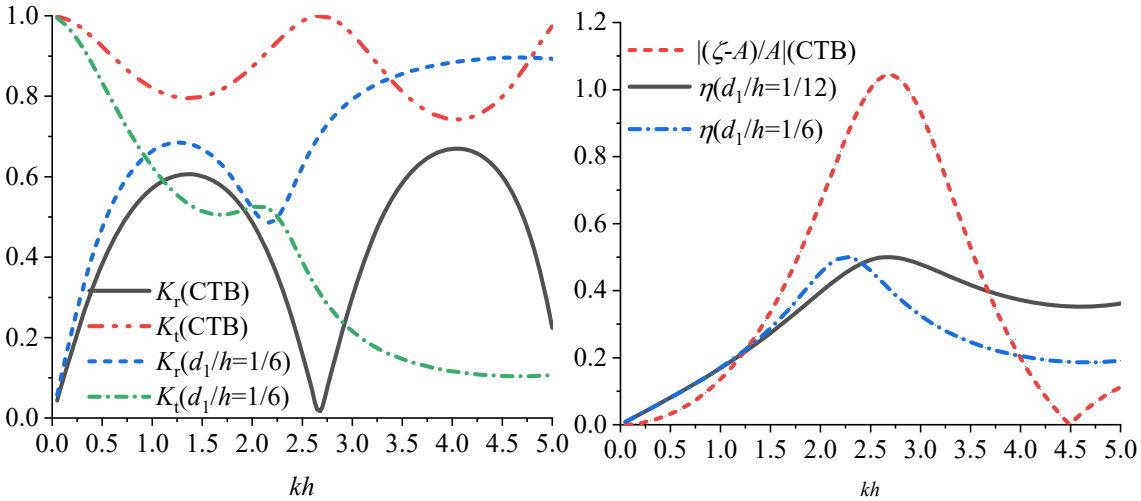

(a) (b)

Fig. 9. Variations of (a) reflection coefficient (K_r) and transmission coefficient (K_t) and (b) CWR (η) and wave amplification factor $(\zeta\text{-}A)/A$ with and without a heaving body.

Interestingly, a special phenomenon of total transmission phenomenon (corresponding to K_t=1.0) occurs at kh=2.65 for cases without the WEC device. The total incident wave energy transmitted to the lee side of the CTB, which is unfavorable to the breakwater. Meanwhile, the wave amplification factor exhibits a peak value at this frequency. Similar phenomena were also found in Fernyhough and Evans (1995), but the physical mechanism of zeros of the reflections is not reported. In the present study, the total transmission coefficient occurs when the breadth of the CTB along the incident wave direction is integral times of half-wavelength $2B \approx nL/2$ ($1 \leqslant n \leqslant \mathrm{int}(\pi/kl)$). This condition may trigger the wave resonance in the x-direction along the incident wave direction, which leads the considerable wave amplification in the wave chamber (as is shown in Fig. 10). As was reported in Dalrymple and Martin (1990) and Mondal et al. (2017), the y-direction resonances perpendicular to the incident wave direction occur when the width $2l$ of the CTB is integral times of wavelength ($kl=n\pi$, n=1, 2$\cdots$). Therefore, if the CTB breadth B is greater than $l/2$, the y-direction resonance occurs right after the total transmission with the increasing dimensionless wavenumber. If the CTB breadth B is less than $l/2$, the total transmission phenomenon would vanish, and only y-direction resonance will occur.

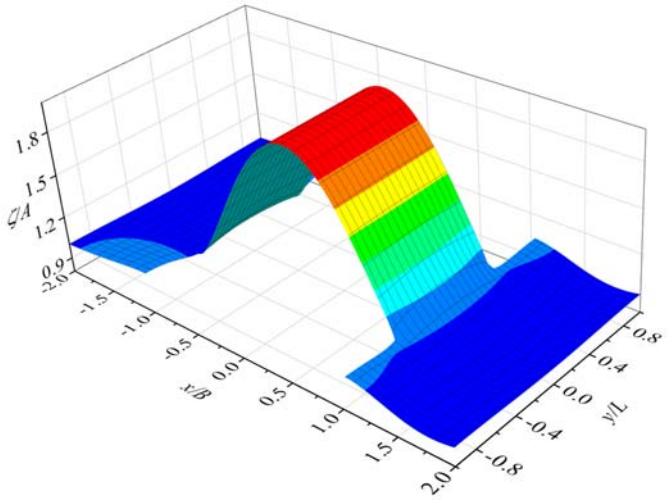

Fig. 10. The relative wave amplitude (ζ/A) of the CTB for the total transmission

The existence of the WEC device canceled the phenomenon of total transmission. It is worthy to note that the location of the peak value of the CWR is close to the location of the total transmission coefficient (i.e., the wave resonance in the x-direction). That means that in order to achieve excellent efficiency, such an integrated system can be designed by the matching

condition of $2B \approx nL/2$ with the wave state at the deployment site.

4.2 Parametric study of the comb-type breakwater

4.2.1 Effect of the breadth of the CTB

Firstly, the effect of the breadth of the CTB is considered in this subsection. Fig. 11 shows the variations of the CWR, K_r, K_t and the dimensionless wave exciting force $F_z/4\rho gAb_2w_2$ for the cases of B/l=1, 5/3, 3 and 20/3. The other geometrical dimensions are w_1/h=1/4, l/h=1/2, d_1/h=1/3, b_2/h=1/3 and b_1/b_3=1. The general trends of the CWR, K_r and K_t against kh are similar to that described in Section 4.1.2. As the breadth increases, stronger oscillations can be found for those curves. This may be due to the fact that more resonance frequencies can be triggered for the wave chamber with a larger breadth (see Fig. 11(b)). Specifically, there only one peak can be found for CTB with the smaller breadth (see Fig. 10), and four peaks are for CTB with a wave chamber of a large breadth (see Fig. 12(c)).

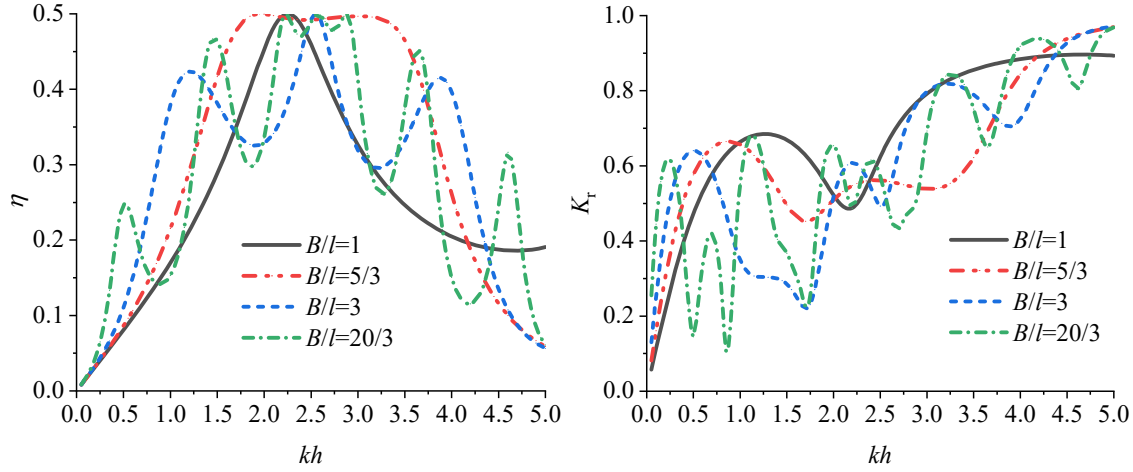

(a)

(b)

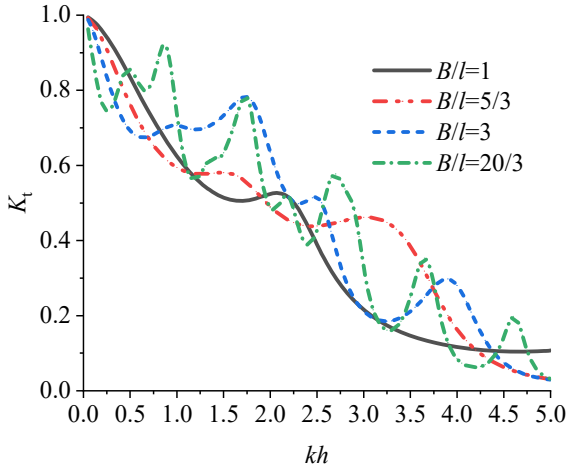

(c)

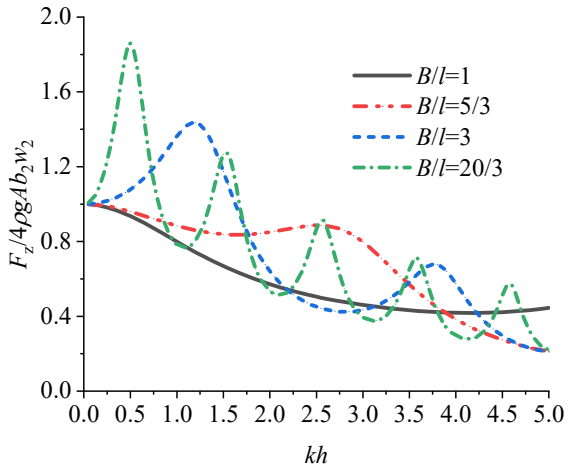

(d)

Fig. 11. Variations of (a) η, (b) K_r, (c) K_t and (d) $F_z/4\rho gAb_2w_2$ versus kh for different cases of breadth of the CTB (w_1/h=1/4, l/h=1/2, d_1/h=1/3, b_2/h=1/3 and b_1/b_3=1, B/l are selected as 1, 5/3, 3 and 20/3).

To study further the heave oscillations, we investigated ζ/A in the wave chamber of the CTB without a heaving body. From the comparisons between Fig. 11(a) and (d) for the case of B/l=3, the first and second of the CWR correspond to the peak of the F_z. The added mass has a dramatic change accompany the occurrence of the peak value of the damping coefficient (as is shown in Fig. 12(a)). The former peak is also agreement with the peak of the ζ/A (as is shown in Fig. 12(b)), which is corresponding to the x-direction wave resonance. And the more water resonances in the wave chamber occur for the latter peak (as is shown in Fig. 12(c)). The second peak of the CWR is attributed to the matching natural frequency ($\omega_{natural}=(K/(M+\mu))^{0.5}$) and the incident wave frequency (Cheng et al., 2014). In summary, the breadth of the CTB influences the wave energy conversion efficiency significantly, mainly caused by the water resonance in the wave chamber and the natural frequency of a heaving body.

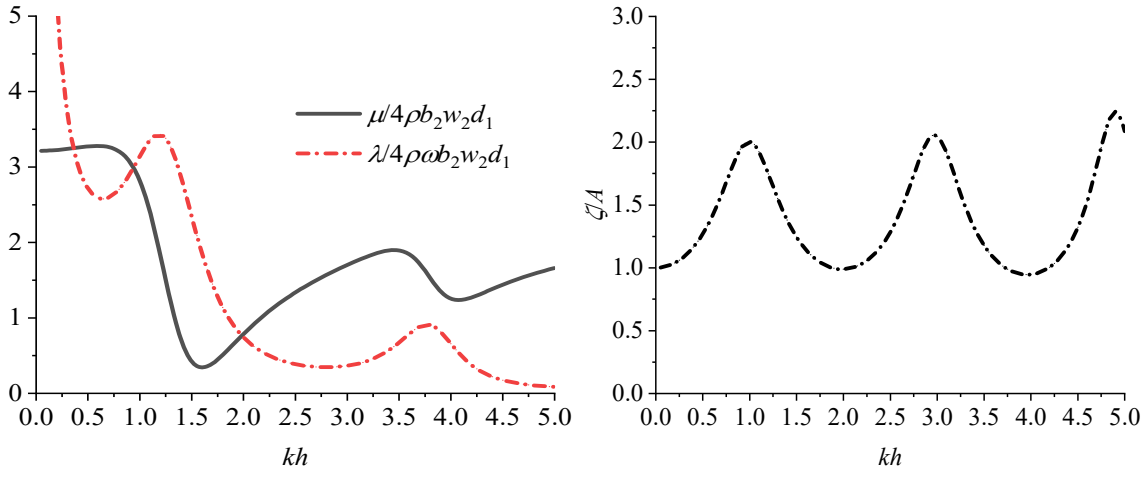

(a) (b)

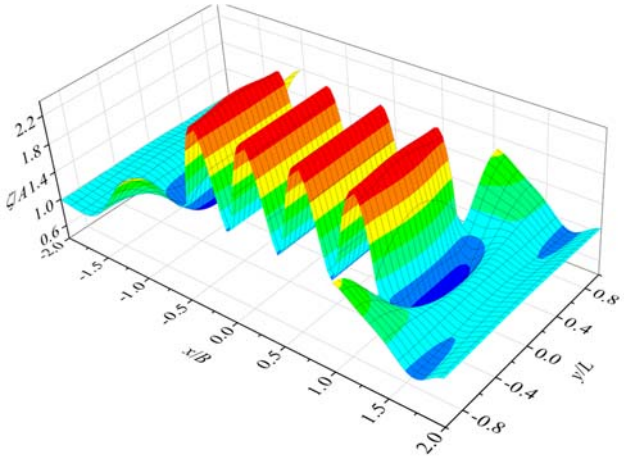

(c)

Fig. 12. Variations of (a) the dimensionless added mass ($\mu/4\rho b_2 w_2 d_1$) and damping coefficient ($\lambda/4\rho\omega b_2 w_2 d_1$) and (b) the relative wave amplitude (ζ/A) versus kh and (c) the relative wave amplitude (ζ/A) of the CTB for the wave resonance for the case of B/l=3.

4.2.2 Effect of the width of the CTB

Results corresponding to different widths (l/h=1/2, 2/3, 5/6, 1 and 7/6) of the integrated system are shown in Fig. 13. The other geometrical parameters are kept constant for b_2/h=1/3, w_2/h=1/3, b_1/b_3=1, d_1/h=1/3 and B/h=1/2. From Fig. 13, it can be found that the K_r, K_t and CWR experience dramatic changes in the high-frequency region. The trend of the CWR presents parabolic changes with the increasing kh and a spike can be found at a critical value k_c. Correspondingly, the reflection coefficient and transmission coefficient exhibit a spike and a valley at the same locations (k=k_c), respectively. For the frequency region of k>k_c, the efficiency of the system is mitigated comparatively. Besides, locations corresponding to the spikes shift to the lower frequency region with increasing CTB width.

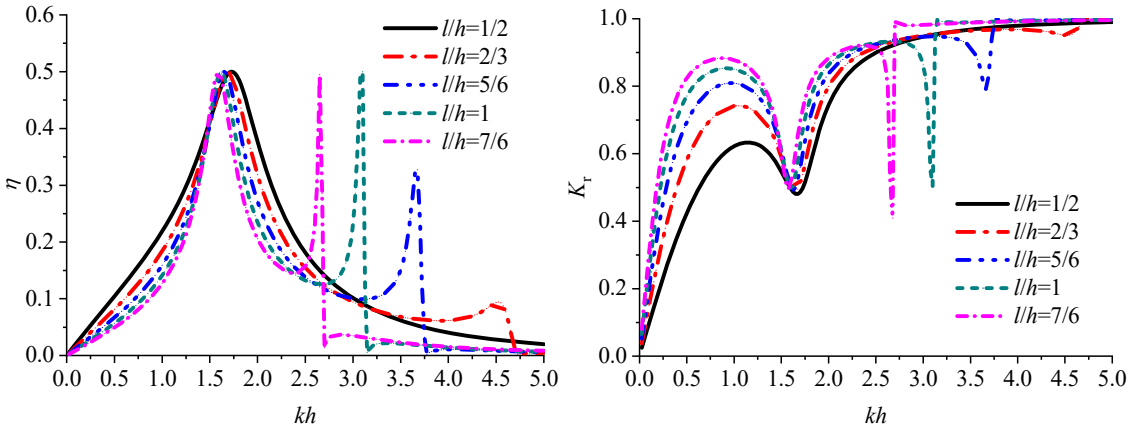

(a) (b)

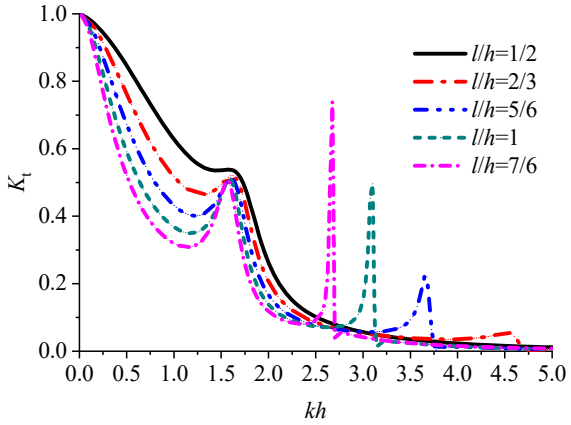

(c)

Fig. 13. Variations of the (a) η, (b) K_r and (c) K_t versus kh with different cases of widths (l/h=1/2, 2/3, 5/6, 1 and 7/6).

The y-direction wave resonance (perpendicular to the incident wave direction) out of the wave chamber (see Fig. 13(c)) may be triggered by conditions of $kl \approx n\pi$, n=1, 2, ⋯ (Fernyhough and Evans, 1995). By checking this condition and the locations of the spike, we found that the critical value k_c corresponds to the y-direction wave resonance out of the wave chamber. This may explain why the k_c shifts to the low-frequency region with increasing CTB width.

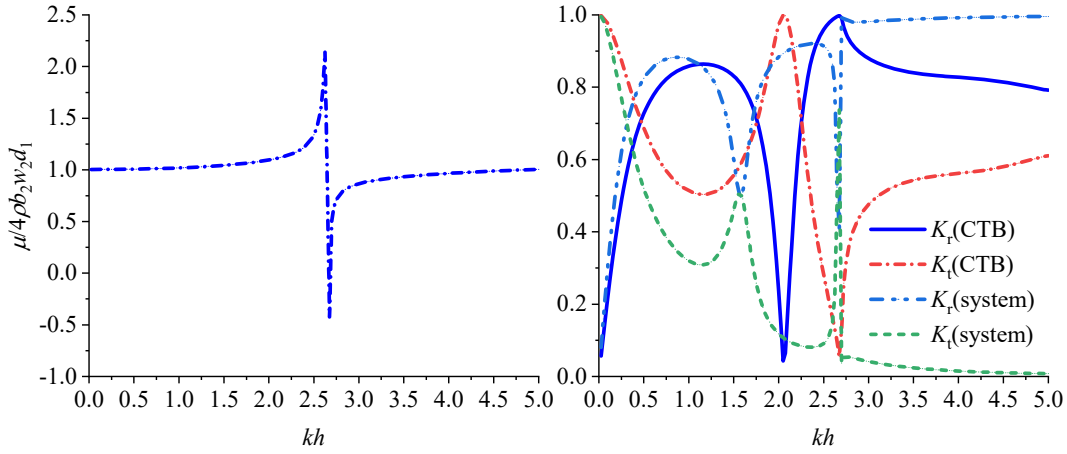

(a) (b)

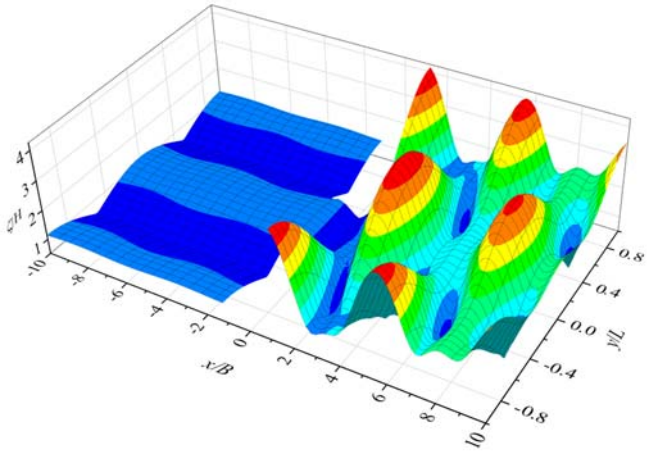

(c)

Fig. 14. Variations of (a) the dimensionless added mass ($\mu/4\rho b_2 w_2 d_1$) and (b) the reflection coefficient (K_r) and transmission coefficient (K_t) with and without a heaving body versus kh and (c) the relative wave amplitude ζ/A of the CTB for the y-direction wave resonance.

As a result of the y-direction wave resonance, the added mass exhibits a dramatic change accompanying the occurrence of negative value at kh=2.65 (as is shown in Fig. 14(a)), which represents the resonance phenomenon (Faltinsen, 2006; Faltinsen et al., 2007). Comparing the results for cases with and without a heaving body (as is shown in Fig. 14(b)), the frequency corresponding to the y-direction resonance has little changes. The distribution of the ζ/A out of the wave chamber is different from that for the total transmission significantly. Mathematically, in Eqs. (50) and (51), when $\kappa_1\pi>pl$, the expression of the K_r and K_t consists of additional items. Those additional items lead to a spike value numerically. Therefore, the y-direction resonance is also called high-order resonance phenomenon (Wang et al., 2018). In summary, the high-order resonance is not beneficial for the wave energy capturing, which should be avoided while designing such a system.

5 Conclusions

In this paper, hydrodynamic performance of a hybrid breakwater-WEC system combining a heaving body WEC and CTB is investigated theoretically. The influence of the geometrical dimensions of both a heaving body and CTB on the performance of the system is emphasized. The physical meaning of the CTB on the efficiency of the device is illustrated. The following conclusions can be drawn:

1) The CWR can approach 77.4% when a heaving body is in the aft end of the wave chamber. Correspondingly, the transmission coefficient is kept as K_t<0.5. Both of the qualified wave attenuation and the excellent wave energy capturing performance can be achieved simultaneously for the present system.

2) Wave resonances both in and out of the wave chamber affect the performance of the WEC significantly. The *x*-direction resonance in the wave chamber ($2B \approx nL/2$) amplified the efficiency of WEC due to wave amplification behavior. However, the frequency corresponding to *y*-direction wave resonance out of the wave chamber ($kl \approx n\pi$) act as a critical value, beyond which the efficiency is mitigated comparatively.

3) Comparing with that of the isolated buoy, the natural frequency of the heaving buoy is modified when it is located at the wave chamber of CTB. The peak efficiency is found to be corresponding to the natural frequency, which is similar to that of the isolated buoy.

The results from the analytical study allow to predict both, the wave attenuation and the wave energy conversion. Thus, the CTB-WEC system can be applicated in the coastal area which is in need of the breakwater function and wave energy utilization. The wave focusing effect due to the wave resonance is beneficial to improve the wave energy conversion efficiency of the WEC, and hence the CTB-WEC provides a benefit in areas with lower wave energy flux density, increasing capturing effectively.

The final PTO efficiency depends on the specific PTO system, the connection style and the sea state. Future large-scale laboratory studies and sea-trail are necessary to establish the achievable efficiency and the practical integration needs, respectively.

In this study no flange is considered at the CTB, a future study will assess the effect of the presence of a flange. Meanwhile, the performance of the system in oblique waves and multi-directional waves will be further investigated.

Acknowledgments

The work is supported by the following project grants, National Natural Science Foundation of China (51509056); Heilongjiang Province Natural Science Fund (E2017028); Fundamental Research Funds for the Central Universities (HEUCFG201813, GK2010260303).

Appendix

The number of the terms in series (i.e., m and n) are selected as M and N. The equations of unknown coefficients are as follows

$$\left[\Xi\right]_{8MN\times 8MN}\left[X\right]_{8MN\times 1}=\left[\bar{X}\right]_{8MN\times 1},$$

$$\left[\Xi\right]_{8MN\times 8MN}\left[X'\right]_{8MN\times 1}=\left[\bar{X}'\right]_{8MN\times 1},$$

$$\left[\Xi\right]_{8MN\times 8MN}=\begin{bmatrix}
\left[\Xi\right]_{MN\times MN}^{1,1} & \left[\Xi\right]_{MN\times MN}^{1,2} & \left[\Xi\right]_{MN\times MN}^{1,3} & 0 & 0 & 0 & 0 & 0\\
\left[\Xi\right]_{MN\times MN}^{2,1} & \left[\Xi\right]_{MN\times MN}^{2,2} & \left[\Xi\right]_{MN\times MN}^{2,3} & 0 & 0 & 0 & 0 & 0\\
0 & \left[\Xi\right]_{MN\times MN}^{3,2} & \left[\Xi\right]_{MN\times MN}^{3,3} & \left[\Xi\right]_{MN\times MN}^{3,4} & \left[\Xi\right]_{MN\times MN}^{3,5} & 0 & 0 & 0\\
0 & \left[\Xi\right]_{MN\times MN}^{4,2} & \left[\Xi\right]_{MN\times MN}^{4,3} & \left[\Xi\right]_{MN\times MN}^{4,4} & \left[\Xi\right]_{MN\times MN}^{4,5} & 0 & 0 & 0\\
0 & 0 & 0 & \left[\Xi\right]_{MN\times MN}^{5,4} & \left[\Xi\right]_{MN\times MN}^{5,5} & \left[\Xi\right]_{MN\times MN}^{5,6} & \left[\Xi\right]_{MN\times MN}^{5,7} & 0\\
0 & 0 & 0 & \left[\Xi\right]_{MN\times MN}^{6,4} & \left[\Xi\right]_{MN\times MN}^{6,5} & \left[\Xi\right]_{MN\times MN}^{6,6} & \left[\Xi\right]_{MN\times MN}^{6,7} & 0\\
0 & 0 & 0 & 0 & 0 & \left[\Xi\right]_{MN\times MN}^{7,6} & \left[\Xi\right]_{MN\times MN}^{7,7} & \left[\Xi\right]_{MN\times MN}^{7,8}\\
0 & 0 & 0 & 0 & 0 & \left[\Xi\right]_{MN\times MN}^{8,6} & \left[\Xi\right]_{MN\times MN}^{8,7} & \left[\Xi\right]_{MN\times MN}^{8,8}
\end{bmatrix},$$

where

$$\left[X\right]_{8MN\times 1}=\left[\left[A_{11},A_{12},\cdots,A_{1N},\cdots,A_{M1},A_{M2},\cdots,A_{MN}\right]^T,\cdots,\left[H_{11},H_{12},\cdots,H_{1N},\cdots,H_{M1},H_{M2},\cdots,H_{MN}\right]^T\right],$$

$$\left[X'\right]_{8MN\times 1}=\left[\left[A'_{11},A'_{12},\cdots,A'_{1N},\cdots,A'_{M1},A'_{M2},\cdots,A'_{MN}\right]^T,\cdots,\left[H'_{11},H'_{12},\cdots,H'_{1N},\cdots,H'_{M1},H'_{M2},\cdots,H'_{MN}\right]^T\right],$$

$$\left[\bar{X}\right]_{8MN\times 1}=\left[\left[\bar{A}_{11},\bar{A}_{12},\cdots,\bar{A}_{1N},\cdots,\bar{A}_{M1},\bar{A}_{M2},\cdots,\bar{A}_{MN}\right]^T,\cdots,\left[\bar{H}_{11},\bar{H}_{12},\cdots,\bar{H}_{1N},\cdots,\bar{H}_{M1},\bar{H}_{M2},\cdots,\bar{H}_{MN}\right]^T\right],$$

$$\left[\bar{X}'\right]_{8MN\times 1}=\left[\left[\bar{A}'_{11},\bar{A}'_{12},\cdots,\bar{A}'_{1N},\cdots,\bar{A}'_{M1},\bar{A}'_{M2},\cdots,\bar{A}'_{MN}\right]^T,\cdots,\left[\bar{H}'_{11},\bar{H}'_{12},\cdots,\bar{H}'_{1N},\cdots,\bar{H}'_{M1},\bar{H}'_{M2},\cdots,\bar{H}'_{MN}\right]^T\right].$$

Considering the condition that $1+NI\leqslant i\leqslant N(I+1)$ and $1+NJ\leqslant j\leqslant N(J+1)$, where I and J=0, 1, 2, $\cdots$, M-1, i and j represent the number of rows and columns in the matrix $\left[\Xi\right]_{8MN\times 8MN}$, the expression of the component in the $\left[\Xi\right]_{8MN\times 8MN}$, $\left[\bar{X}\right]_{8MN\times 1}$ and $\left[\bar{X}'\right]_{8MN\times 1}$ are as follow

$$\left[\Xi\right]_{i,j}^{1,1}=\begin{cases}\beta_{J+1,I+1}\alpha_{i-N*I,i-N*I}, i-j=(I-J)N,\\ 0, i-j\neq(I-J)N,\end{cases}$$

$$\left[\Xi\right]_{i,j}^{1,2}=\left[\Xi\right]_{i,j}^{1,3}=\begin{cases}-\sigma_{I+1,I+1}\alpha_{i-N*I,i-N*I}, I=J, i=j,\\ 0, I=J, i\neq j,\\ 0, I\neq J,\end{cases}$$

1 $$[\Xi]_{i,j}^{2,1}=\begin{cases}\overline{\sigma}_{I+1,I+1}p_{I+1,i-N^*I}\alpha_{i-N^*I,i-N^*I}, I=J, i=j,\\ 0, I=J, i\neq j,\\ 0, I\neq J,\end{cases}$$

2 $$[\Xi]_{i,j}^{2,2}=\begin{cases}-\beta_{I+1,J+1}\overline{p}_{J+1,,i-N^*I}\tanh\overline{p}_{J+1,,i-N^*I}b_3\alpha_{i-N^*I,i-N^*I}, i-j=(I-J)N,\\ 0, i-j\neq(I-J)N,\end{cases}$$

3 $$[\Xi]_{i,j}^{2,3}=\begin{cases}-\beta_{I+1,J+1}\overline{p}_{J+1,,i-N^*I}\coth\overline{p}_{J+1,,i-N^*I}b_3\alpha_{i-N^*I,i-N^*I}, i-j=(I-J)N,\\ 0, i-j\neq(I-J)N,\end{cases}$$

4 $$[\Xi]_{i,j}^{3,2}=\begin{cases}\sigma_{I+1,I+1}\tau_{j-N^*J,i-N^*I}, I=J,\\ 0, I\neq J,\end{cases}$$

5 $$[\Xi]_{i,j}^{3,3}=\begin{cases}-\sigma_{I+1,I+1}\tau_{j-N^*J,i-N^*I}, I=J,\\ 0, I\neq J,\end{cases}$$

6 $$[\Xi]_{i,j}^{3,4}=[\Xi]_{i,j}^{3,5}=\begin{cases}-\sigma_{I+1,I+1}U_{i-N^*I,i-N^*I}, I=J, i=j,\\ 0, I=J, i\neq j,\\ 0, I\neq J,\end{cases}$$

7 $$[\Xi]_{i,j}^{4,2}=\begin{cases}-\sigma_{I+1,I+1}\overline{p}_{I+1,i-N^*I}\tanh\overline{p}_{I+1,i-N^*I}b_3\alpha_{i-N^*I,i-N^*I}, I=J, i=j,\\ 0, I=J, i\neq j,\\ 0, I\neq J,\end{cases}$$

8 $$[\Xi]_{i,j}^{4,3}=\begin{cases}\sigma_{I+1,I+1}\overline{p}_{I+1,i-N^*I}\coth\overline{p}_{I+1,i-N^*I}b_3\alpha_{i-N^*I,i-N^*I}, I=J, i=j,\\ 0, I=J, i\neq j,\\ 0, I\neq J,\end{cases}$$

9 $$[\Xi]_{i,j}^{4,4}=\begin{cases}0, I=J=0, j=1,\\ -\sigma_{I+1,I+1}q_{I+1,j-N^*J}\tanh q_{I+1,j-N^*J}b_2\tau_{i-N^*I,j-N^*J}, I=J=0, j\neq 1,\\ -\sigma_{I+1,I+1}q_{I+1,j-N^*J}\tanh q_{I+1,j-N^*J}b_2\tau_{i-N^*I,j-N^*J}, I=J\neq 0,\\ 0, I\neq J,\end{cases}$$

10 $$[\Xi]_{i,j}^{4,5}=\begin{cases}-\dfrac{\sigma_{11}\tau_{i,1}}{b_2}, I=J=0, j=1,\\ -\sigma_{I+1,I+1}q_{I+1,j-N^*J}\coth q_{I+1,j-N^*J}b_2\tau_{i-N^*I,j-N^*J}, I=J=0, j\neq 1,\\ -\sigma_{I+1,I+1}q_{I+1,j-N^*J}\coth q_{I+1,j-N^*J}b_2\tau_{i-N^*I,j-N^*J}, I=J\neq 0,\\ 0, I\neq J,\end{cases}$$

11 $$[\Xi]_{i,j}^{5,4}=\begin{cases}\sigma_{I+1,I+1}U_{i-N^*I,i-N^*I}, I=J, i=j,\\ 0, I=J, i\neq j,\\ 0, I\neq J,\end{cases}$$

1 $$[\Xi]_{i,j}^{5,5}=\begin{cases}-\sigma_{I+1,I+1}U_{i-N^*I,i-N^*I}, I=J, i=j,\\ 0, I=J, i\neq j,\\ 0, I\neq J,\end{cases}$$

2 $$[\Xi]_{i,j}^{5,6}=[\Xi]_{i,j}^{5,7}=\begin{cases}-\sigma_{I+1,I+1}\tau_{j-N^*J,i-N^*I}, I=J,\\ 0, I\neq J,\end{cases}$$

3 $$[\Xi]_{i,j}^{6,4}=\begin{cases}0, I=J=0, j=1,\\ -\sigma_{I+1,I+1}q_{I+1,j-N^*J}\tanh q_{I+1,j-N^*J}b_2\tau_{i-N^*I,j-N^*J}, I=J=0, j\neq 1,\\ -\sigma_{I+1,I+1}q_{I+1,j-N^*J}\tanh q_{I+1,j-N^*J}b_2\tau_{i-N^*I,j-N^*J}, I=J\neq 0,\\ 0, I\neq J,\end{cases}$$

4 $$[\Xi]_{i,j}^{6,5}=\begin{cases}\dfrac{\sigma_{11}\tau_{i,1}}{b_2}, I=J=0, j=1,\\ \sigma_{I+1,I+1}q_{I+1,j-N^*J}\coth q_{I+1,j-N^*J}b_2\tau_{i-N^*I,j-N^*J}, I=J=0, j\neq 1,\\ \sigma_{I+1,I+1}q_{I+1,j-N^*J}\coth q_{I+1,j-N^*J}b_2\tau_{i-N^*I,j-N^*J}, I=J\neq 0,\\ 0, I\neq J,\end{cases}$$

5 $$[\Xi]_{i,j}^{6,6}=\begin{cases}-\sigma_{I+1,I+1}\overline{p}_{I+1,i-N^*I}\tanh \overline{p}_{I+1,i-N^*I}b_1\alpha_{i-N^*I,i-N^*I}, I=J, i=j,\\ 0, I=J, i\neq j,\\ 0, I\neq J,\end{cases}$$

6 $$[\Xi]_{i,j}^{6,7}=\begin{cases}-\sigma_{I+1,I+1}\overline{p}_{I+1,i-N^*I}\coth \overline{p}_{I+1,i-N^*I}b_1\alpha_{i-N^*I,i-N^*I}, I=J, i=j,\\ 0, I=J, i\neq j,\\ 0, I\neq J,\end{cases}$$

7 $$[\Xi]_{i,j}^{7,6}=\begin{cases}\sigma_{I+1,I+1}\alpha_{i-N^*I,i-N^*I}, I=J, i=j,\\ 0, I=J, i\neq j,\\ 0, I\neq J,\end{cases}$$

8 $$[\Xi]_{i,j}^{7,7}=\begin{cases}-\sigma_{I+1,I+1}\alpha_{i-N^*I,i-N^*I}, I=J, i=j,\\ 0, I=J, i\neq j,\\ 0, I\neq J,\end{cases}$$

9 $$[\Xi]_{i,j}^{7,8}=\begin{cases}-\beta_{J+1,I+1}\alpha_{i-N^*I,i-N^*I}, i-j=(I-J)N,\\ 0, i-j\neq(I-J)N,\end{cases}$$

10 $$[\Xi]_{i,j}^{8,6}=\begin{cases}-\beta_{I+1,J+1}\overline{p}_{J+1,i-N^*I}\tanh \overline{p}_{J+1,i-N^*I}b_1\alpha_{i-N^*I,i-N^*I}, i-j=(I-J)N,\\ 0, i-j\neq(I-J)N,\end{cases}$$

11 $$[\Xi]_{i,j}^{8,7}=\begin{cases}\beta_{I+1,J+1}\overline{p}_{J+1,i-N^*I}\coth \overline{p}_{J+1,i-N^*I}b_1\alpha_{i-N^*I,i-N^*I}, i-j=(I-J)N,\\ 0, i-j\neq(I-J)N,\end{cases}$$

$$\left[\Xi\right]_{i,j}^{8,8}=\begin{cases}\overline{\sigma}_{I+1,I+1}p_{I+1,i-N*I}\alpha_{i-N*I,i-N*I},I=J,i=j,\\0,I=J,i\neq j,\\0,I\neq J,\end{cases}$$

$$\left[\overline{X}\right]_{i,1}^{2}=\begin{cases}\mathrm{i}\kappa_1\alpha_{11}L_{I+1},i=N*I+1,\\0,i\neq N*I+1,\end{cases}$$

$$\left[\overline{X}\right]_{i,1}^{3}=\begin{cases}-\mathrm{e}^{\mathrm{i}\kappa_1 2b_3}\sigma_{11}\tau_{1i},I=0,\\0,I\neq 0,\end{cases}\left[\overline{X}'\right]_{i,1}^{3}=\begin{cases}\dfrac{\mathrm{i}\omega}{gA}\sigma_{11}W_i,I=0,\\0,I\neq 0,\end{cases}$$

$$\left[\overline{X}\right]_{i,1}^{4}=\begin{cases}\mathrm{i}\kappa_1\mathrm{e}^{\mathrm{i}\kappa_1 2b_3}\sigma_{11}\alpha_{11},i=1,\\0,i\neq 1,\end{cases}\left[\overline{X}'\right]_{i,1}^{4}=\begin{cases}-\dfrac{\mathrm{i}\omega}{gA}\dfrac{b_2}{h-d_1}\sigma_{11}\tau_{i1},I=0,\\0,I\neq 0,\end{cases}$$

$$\left[\overline{X}\right]_{i,1}^{5}=\begin{cases}\mathrm{e}^{\mathrm{i}\kappa_1(b_2+r_4)}\tau_{1i}\sigma_{11},I=0,\\0,I\neq 0,\end{cases}\left[\overline{X}'\right]_{i,1}^{5}=\begin{cases}-\dfrac{\mathrm{i}\omega}{gA}\sigma_{11}W_i,I=0,\\0,I\neq 0,\end{cases}$$

$$\left[\overline{X}\right]_{i,1}^{6}=\begin{cases}-\mathrm{i}\kappa_1\mathrm{e}^{\mathrm{i}\kappa_1(b_2+r_4)}\alpha_{11}\sigma_{11},i=1,\\0,i\neq 1,\end{cases}\left[\overline{X}'\right]_{i,1}^{6}=\begin{cases}-\dfrac{\mathrm{i}\omega}{gA}\dfrac{b_2}{h-d_1}\sigma_{11}\tau_{i1},I=0,\\0,I\neq 0,\end{cases}$$

$$\left[\overline{X}\right]_{i,1}^{8}=\begin{cases}-\mathrm{i}\kappa_1\mathrm{e}^{\mathrm{i}\kappa_1(r_2+r_4)}\alpha_{11}L_{I+1},i=1+N*I,\\0,i\neq 1+N*I,\end{cases}$$

where the unknown functions can be expressed by

$$\beta_{mv}=\int_{-w_2}^{w_2}C_m(y)\overline{C}_v(y)dy=\begin{cases}(-1)^{m-v}w_2,\gamma_m=\overline{\gamma}_v\neq 0,\\\dfrac{2(-1)^{m-1}\gamma_m\sin\gamma_m w_2}{\gamma_m^2-\overline{\gamma}_v^2},\gamma_m\neq\overline{\gamma}_v,\\2w_2,\gamma_m=\overline{\gamma}_v=0,\end{cases}$$

$$L_v=\begin{cases}2(-1)^v\dfrac{\sin\gamma_v w_2}{\gamma_v},v\neq 1,\\2(l-w_2),v=1,\end{cases}$$

$$\tau_{nu}=\int_{-h}^{-d_1}Z_n(z)\varphi_u(z)dz=\frac{(-1)^{u-1}k_n\sin k_n(h-d_1)}{(k_n^2-\mu_u^2)\cos k_n h},$$

$$W_u = \begin{cases} \dfrac{(h-d_1)^2}{6} - \dfrac{b_2^2}{2}, u = 1, \\ \dfrac{(-1)^{u-1}}{\mu_u^2}, u \neq 1. \end{cases}$$

The expression of the vertical exciting force F_z, added mass μ and damping coefficient λ are expressed as

$$F_z = 4\rho g A w_2 \left\{ b_2 D_{11} + \sum_{n=2}^{\infty} D_{1n} \frac{\tanh q_{1n} b_2}{q_{1n}} (-1)^{n-1} \right\},$$

$$\mu = \mathrm{Re}\left\{ -\frac{\mathrm{i}\rho g A}{\omega} \left\{ \left[4 b_2 w_2 D'_{11} + 4 w_2 \sum_{n=2}^{\infty} D'_{1n} \frac{\tanh q_{1n} b_2}{q_{1n}} (-1)^{n-1} \right] \right\} + 2 w_2 \left[(h-d_1) b_2 - \frac{b_2^3}{3(h-d_1)} \right] \right\},$$

$$\lambda = \mathrm{Im}\left\{ -\mathrm{i}\rho g A \left\{ \left[4 b_2 w_2 D'_{11} + 4 w_2 \sum_{n=2}^{\infty} D'_{1n} \frac{\tanh q_{1n} b_2}{q_{1n}} (-1)^{n-1} \right] \right\} + 2 w_2 \left[(h-d_1) b_2 - \frac{b_2^3}{3(h-d_1)} \right] \right\}.$$

References

Brito-Melo, A., Neumann, F., Sarmento, A.J.N.A., 2007. Full-Scale Data Assessment in OWC Pico Plant. 17th 2007 International Offshore and Polar Engineering Conference, ISOPE 2007, Lisbon.

Cascajo, R., García, E., Quiles, E., Correcher, A., Morant, F., 2019. Integration of Marine Wave Energy Converters into Seaports: A Case Study in the Port of Valencia. Energies. 12(5).

Chen, Y., Niu, G., Ma, Y., Zhou, P., He, Y.Q., 2019. Study On Hydrodynamics of a New Comb-type Floating Breakwater Fixed On the Water Surface. 2018 International Symposium on Architecture Research Frontiers and Ecological Environment, ARFEE 2018.

Chen, Q., Zang, J., Birchall, J., Ning, D., Zhao, X., Gao, J., 2020. On the Hydrodynamic Performance of a Vertical Pile-Restrained WEC-type Floating Breakwater. Renewable Energy. 146, 414-425.

Cheng, Z.S., Yang, J.M., Hu, Z.Q., Xiao, L.F., 2014. Frequency/Time Domain Modeling of a Direct Drive Point Absorber Wave Energy Converter. Science China: Physics, Mechanics and Astronomy. 57(2), 311-320.

Count, B.M., 1984. The Influence of Projecting Sidewalls On the Hydrodynamic Performance of Wave-Energy Devices. Journal of Fluid Mechanics. 145(7), 361-376.

Dalrymple, R.A., Martin, P.A., 1990. Wave Diffraction through Offshore Breakwaters. Journal of Waterway, Port, Coastal and Ocean Engineering. 116(6), 727-741.

Daniel Raj, D., Sundar, V., Sannasiraj, S.A., 2019. Enhancement of Hydrodynamic Performance of an Oscillating Water Column with Harbour Walls. Renewable Energy. 132, 142-156.

Deng, Z., Huang, Z., Law, A.W.K., 2014. Wave Power Extraction From a Bottom-Mounted Oscillating Water Column Converter with a V-shaped Channel. Proceedings of the Royal Society A: Mathematical, Physical and Engineering Sciences. 470(2167).

Dong, G.H., Li, Y.C., Sun, Z.C., Sun, Y., Niu, E.Z., Mao, K., 2003. Interaction Between Waves and a Comb-Type Breakwater. China Ocean Engineering. 17(4), 517.

Faltinsen, O.M., 2006. Hydrodynamics of High-Speed Marine Vehicles, Cambridge University Press.

Faltinsen, O.M., Rognebakke, O.F., Timokha, A.N., 2007. Two-Dimensional Resonant Piston-Like Sloshing in a Moonpool. Journal of Fluid Mechanics. 575, 359-397.

Fang, Z., Cheng, L., Zhang, N., 2010. Development of 3-D Numerical Wave Tank and Applications On Comb-Type Breakwater. ASME 2010 29th International Conference on Ocean, Offshore and Arctic Engineering, OMAE2010, Shanghai.

Fang, Z., Zhang, N.C., Zang, Z.P., 2012. Experimental and Numerical Study On Hydrodynamic Performance of Impermeable Comb-Type Breakwater. Chuan Bo Li Xue/Journal of Ship Mechanics. 16(6), 632-645.

Fernyhough, M., Evans, D.V., 1995. Scattering by a Periodic Array of Rectangular Blocks. Journal of Fluid Mechanics. 305, 263-279.

He, F., Zhang, H., Zhao, J., Zheng, S., Iglesias, G., 2019. Hydrodynamic Performance of a Pile-Supported OWC Breakwater: An Analytical Study. Applied Ocean Research. 88, 326-340.

Henriques, J.C.C., Sheng, W., Falcão, A.F.O., Gato, L.M.C., 2017. A Comparison of Biradial and Wells Air Turbines On the Mutriku Breakwater OWC Wave Power Plant. ASME 2017 36th International Conference on Ocean, Offshore and Arctic Engineering, OMAE 2017.

Howe, D., Nader, J.R., 2017. OWC WEC Integrated within a Breakwater Versus Isolated: Experimental and Numerical Theoretical Study. International Journal of Marine Energy. 20, 165-182.

Ikoma, T., Masuda, K., Omori, H., Osawa, H., Maeda, H., 2016. Improvement of Performance of Wave Power Conversion Due to the Projecting Walls for Oscillating Water Column Type Wave Energy Converter. Journal of Offshore Mechanics and Arctic Engineering. 138(2).

Ji, C., Yuan, Z., 2015. Experimental Study of a Hybrid Mooring System. Journal of Marine Science and Technology (Japan). 20(2), 213-225.

Koutandos, E., Prinos, P., Gironella, X., 2005. Floating Breakwaters Under Regular and Irregular Wave Forcing: Reflection and Transmission Characteristics. Journal of Hydraulic Research 43(2), 174-188.

Kuo, Y.S., Chung, C.Y., Hsiao, S.C., Wang, Y.K., 2017. Hydrodynamic Characteristics of Oscillating Water Column Caisson Breakwaters. Renewable Energy. 103, 439-447.

Li, Y.C., Sun, Z.C., Xu, S.Q., 2002. Hydraulic Characteristics of Comb Caisson Breakwater. Journal of Hydrodynamics. 17.

Liu, J., Lin, G., 2013. Scaled Boundary FEM Solution of Short-Crested Wave Interaction with a Concentric Structure with Double-Layer Arc-Shaped Perforated Cylinders. Computers and Fluids. 79, 82-104.

Liu, J., Lin, G., Li, J., 2012. Short-Crested Waves Interaction with a Concentric Cylindrical Structure with Double-Layered Perforated Walls. Ocean Engineering. 40, 76-90.

Liu, Y., Faraci, C., 2014. Analysis of Orthogonal Wave Reflection by a Caisson with Open Front Chamber Filled with Sloping Rubble Mound. Coastal Engineering. 91, 151-163.

Lovas, S., Mei, C.C., Liu, Y., 2010. Oscillating Water Column at a Coastal Corner for Wave Power Extraction. Applied Ocean Research. 32(3), 267-283.

Madhi, F., Yeung, R.W., 2018. On Survivability of Asymmetric Wave-Energy Converters in Extreme Waves. Renewable Energy. 119, 891-909.

Martinelli, L., Ruol, P., Favaretto, C., Wang, A.M., Chung, J.S., Kokkinis, T., Muskulus, M., 2016. Hybrid Structure Combining a Wave Energy Converter and a Floating Breakwater. 26th Annual International Ocean and Polar Engineering Conference, ISOPE 2016.

Margheritini, L., Vicinanza, D., Frigaard, P., 2009. SSG Wave Energy Converter: Design, Reliability and Hydraulic Performance of an Innovative Overtopping Device. Renewable Energy. 34(5), 1371-1380.

Melikoglu, M., 2018. Current Status and Future of Ocean Energy Sources: A Global Review. Ocean Engineering. 148, 563-573.

Miao, G.P., Cheng, J.S., You, Y.X., Wang, J.Q., 2005. Wave Defending Effects of V-Type Bottom-Mounted

Breakwaters. China Ocean Engineering. 19(2), 195-204.
Michele, S., Sammarco, P., D'Errico, M., 2016. The Optimal Design of a Flap Gate Array in Front of a Straight Vertical Wall: Resonance of the Natural Modes and Enhancement of the Exciting Torque. Ocean Engineering. 118, 152-164.
Mondal, R., Takagi, K., Wada, R., 2017. Diffraction Problem of a Floating Breakwater with an Array of Small Ports. Journal of Marine Science and Technology (Japan). 22(3), 459-469.
Moretti, G., Malara, G., Scialò, A., Daniele, L., Romolo, A., Vertechy, R., Fontana, M., Arena, F., 2020. Modelling and Field Testing of a Breakwater-Integrated U-OWC Wave Energy Converter with Dielectric Elastomer Generator. Renewable Energy. 146, 628-642.
Mustapa, M.A., Yaakob, O.B., Ahmed, Y.M., Rheem, C., Koh, K.K., Adnan, F.A., 2017. Wave Energy Device and Breakwater Integration: A Review. Renewable and Sustainable Energy Reviews. 77, 43-58.
Ning, D., Zhao, X., Göteman, M., Kang, H., 2016. Hydrodynamic Performance of a Pile-Restrained WEC-type Floating Breakwater: An Experimental Study. Renewable Energy. 95, 531-541.
Niu, E.Z., Ma, D.T., Sun, S.C., 2003. The Novel Comb-Type Breakwater. China Civil Engineering Journal. 36(10), 51-56.
Niu, G., Yang, Y., Nie, X., Liu, S., Wang, X., 2018. Experimental Study On Hydrodynamic Characteristics of a New Comb-Type Floating Breakwater. 28th International Ocean and Polar Engineering Conference, ISOPE 2018.
Parmeggiani, S., Kofoed, J.P., Friis-Madsen, E., 2013. Experimental Update of the Overtopping Model Used for the Wave Dragon Wave Energy Converter. Energies. 6(4), 1961-1992.
Pérez-Collazo, C., Greaves, D., Iglesias, G., 2015. A Review of Combined Wave and Offshore Wind Energy. Renewable and Sustainable Energy Reviews. 42, 141-153.
Ram, K.R., Ahmed, M.R., Zullah, M.A., Lee, Y., 2016. Experimental Studies On the Flow Characteristics in an Inclined Bend-Free OWC Device. Journal of Ocean Engineering and Science. 1(1), 77-83.
Reabroy, R., Zheng, X., Zhang, L., Zang, J., Yuan, Z., Liu, M., Sun, K., Tiaple, Y., 2019. Hydrodynamic Response and Power Efficiency Analysis of Heaving Wave Energy Converter Integrated with Breakwater. Energy Conversion and Management. 195, 1174-1186.
Rezanejad, K., Bhattacharjee, J., Guedes Soares, C., 2013. Stepped Sea Bottom Effects On the Efficiency of Nearshore Oscillating Water Column Device. Ocean Engineering. 70, 25-38.
Rezanejad, K., Souto-Iglesias, A., Guedes Soares, C., 2019. Experimental Investigation On the Hydrodynamic Performance of an L-shaped Duct Oscillating Water Column Wave Energy Converter. Ocean Engineering., 388-398.
Saadat, Y., Fernandez, N., Samimi, A., Alam, M.R., Shakeri, M., Ghorbani, R., 2016. Investigating of Helmholtz Wave Energy Converter. Renewable Energy. 87, 67-76.
Saadat, Y., Fernandez, N., Ghorbani, R., 2013. The Wave Energy Converter Based On Helmholtz Mode, Inspired by Nature. ASME 2013 32nd International Conference on Ocean, Offshore and Arctic Engineering, OMAE 2013, Nantes.
Sarkar, D., Renzi, E., Dias, F., 2015. Effect of a Straight Coast On the Hydrodynamics and Performance of the Oscillating Wave Surge Converter. Ocean Engineering. 105, 25-32.
Tul Huda Ahmad, N.H., Zamri Ibrahim, M., Rahman, S.J.A., Albani, A., Mohad, S., 2019. The Development of Wave Energy Converter System Using Hydraulic Power Take Off at Terengganu Shoreline. 2018 International Conference on Green Energy for Sustainable Development, ICUE 2018.
Vicinanza, D., Contestabile, P., Quvang Harck Nørgaard, J., Lykke Andersen, T., 2014. Innovative Rubble Mound

Breakwaters for Overtopping Wave Energy Conversion. Coastal Engineering. 88, 154-170.
Wang, X., Liu, Y., Liang, B., 2018. Analysis of Oblique Wave Interaction with a Comb-Type Caisson Breakwater. Journal of Ocean University of China. 17(2), 281-290.
Wang, X., Liu, Y., Lu, L., 2019. Analytical Solution of Oblique Wave Interacting with a Periodic Array of Specific Caissons Connected with Partially Immersed Thin Walls (Comb-Type). Ocean Engineering. 186, 106107.
Wilberforce, T., El Hassan, Z., Durrant, A., Thompson, J., Soudan, B., Olabi, A.G., 2019. Overview of Ocean Power Technology. Energy. 175, 165-181.
Zang, Z., Fang, Z., Zhang, N., 2018. Flow Mechanism of Impulsive Wave Forces and Improvement On Hydrodynamic Performance of a Comb-Type Breakwater. Coastal Engineering. 133, 142-158.
Zhang, H., Zhou, B., Vogel, C., Willden, R., Zang, J., Geng, J., 2020. Hydrodynamic Performance of a Dual-Floater Hybrid System Combining a Floating Breakwater and an Oscillating-Buoy Type Wave Energy Converter. Applied Energy. 259.
Zhang, H., Zhou, B., Vogel, C., Willden, R., Zang, J., Zhang, L., 2020. Hydrodynamic Performance of a Floating Breakwater as an Oscillating-Buoy Type Wave Energy Converter. Applied Energy. 257.
Zhang, T., Wang, Q., Wang, S., 2005. Research On the Flange Plate of the Comb-Type Caisson. MTS/IEEE OCEANS, 2005, Washington, DC.
Zhang, C., Ning, D., 2019. Hydrodynamic Study of a Novel Breakwater with Parabolic Openings for Wave Energy Harvest. Ocean Engineering. 182, 540-551.
Zhao, X., Ning, D., 2018. Experimental Investigation of Breakwater-Type WEC Composed of Both Stationary and Floating Pontoons. Energy. 155, 226-233.
Zhao, X.L., Ning, D.Z., Zou, Q.P., Qiao, D.S., Cai, S.Q., 2019. Hybrid Floating breakwater-WEC System: A Review. Ocean Engineering. 186, 106126.
Zhao, X., Ning, D., Zhang, C., Kang, H., 2017. Hydrodynamic Investigation of an Oscillating Body Wave Energy Converter Integrated into a Pile-Restrained Floating Breakwater. Energies. 10(5).
Zhao, X.L., Ning, D.Z., Liang, D.F., 2019. Experimental Investigation On Hydrodynamic Performance of a Breakwater-Integrated WEC System. Ocean Engineering. 25-32.
Zheng, S., Zhang, Y., Iglesias, G., 2019. Coast/Breakwater-Integrated OWC: A Theoretical Model. Marine Structure. 66, 121-135.